Research Paper

# Dynamics of Jupiter's equatorial zone: Instability analysis and a mechanism for Y-shaped structures

Masoud Rostami [a,b,*], Bijan Fallah [c], Farahnaz Fazel-Rastgar [d]

[a] *Potsdam Institute for Climate Impact Research (PIK), Member of the Leibniz Association, Potsdam, Germany*
[b] *Laboratoire de Météorologie Dynamique, Sorbonne University (SU)/ Ecole Normale Supérieure (ENS)/CNRS, 75005 Paris, France*
[c] *Deutsches Klimarechenzentrum GmbH (DKRZ), Bundesstraße 45a, D-20146 Hamburg, Germany*
[d] *School of Chemistry and Physics, University of KwaZulu Natal, Durban 4000, South Africa*

ABSTRACT

Jupiter's Equatorial Zone (EZ) is characterized by atmospheric dynamics influenced by strong zonal jets. Initially, we perform a linear stability analysis of two-layer geostrophic flows to explore the growth and evolution of instabilities associated with equatorial jets. Stability diagrams reveal that the most unstable baroclinic modes shift to lower wavenumbers with increasing zonal velocities, indicating sensitivity to the strength of the zonal wind. We show notable differences in phase velocities between barotropic and baroclinic jets. Phase portraits of the dynamic structures of various wave types, including barotropic and baroclinic Kelvin waves, Yanai waves, Rossby waves, and inertia-gravity waves, are illustrated in this analysis. Subsequently, we employ a two-layer moist convective Rotating Shallow Water (2mcRSW) model to investigate the nonlinear interactions between ammonia-driven convective processes in the shallow upper atmosphere and large-scale atmospheric features in Jupiter's EZ. We analyze the evolution of nonlinear instabilities in moist-convective flows by perturbing a background zonal velocity field with the most unstable mode. Findings include the amplification of cyclonic and anticyclonic vortices driven by moist convection at the boundaries of the zonal jets and the suppression of convective vortices in equatorial bright zones. This study underscores the role of moist convection in generating upper atmosphere cloud clusters and lightning patterns, as well as the chevron-shaped pattern observed on the poleward side of the zonal jets. Finally, we propose a novel mechanism for the formation of Y-shaped structures on Jupiter, driven by equatorial modons coupled with convectively baroclinic Kelvin waves (CCBCKWs). This mechanism suggests that Y-shaped structures result from large-scale localized heating in a diabatic environment, which, upon reaching a critical threshold of negative pressure or positive buoyancy anomaly, generates a *hybrid structure*. This *hybrid structure* consists of a *quasi equatorial modon*, a coherent dipolar structure, coupled with a CCBCKW that propagates eastward in a self-sustaining and self-propelled manner. Initially, the hybrid moves steadily eastward; however, the larger phase speed of the CCBCKW eventually leads to its detachment from the *quasi equatorial modon*. The lifetime of this coupled structure varies from interseasonal to seasonal timescales. Moist convection is a necessary condition for triggering the eastward-propagating structure.

**Key Points**:

(1) **Stability Analysis Insights:** The study reveals the most unstable modes, dispersion relation, and their phase portraits in Jupiter's Equatorial Zone, with distinct patterns observed in barotropic and baroclinic stability analyses.

(2) **Moist Convection Effects:** Nonlinear simulations show that moist convection amplifies cyclonic and anticyclonic vortices, significantly impacting large-scale circulations in the vicinity of zonal jets and the poleward drift of emerged vortices.

(3) **Y-shaped Cloud Formation:** Y-shaped cloud structures on Jupiter are explained by the equatorial adjustment of a large-scale localized warm pool in a diabatic environment, which leads to a *hybrid structure* of baroclinic modons and Kelvin waves, with an interseasonal to seasonal lifetime.

* Correspondence to: Potsdam Institute for Climate Impact Research (PIK), Member of the Leibniz Association, P.O. Box 6012 03, D-14412 Potsdam, Germany

*E-mail addresses:* rostami@pik-potsdam.de, rostami@lmd.ipsl.fr (M. Rostami).

## 1. Introduction

This study investigates the linear and nonlinear instabilities triggered by synoptic-scale equatorial disturbances under idealized diabatic and adiabatic conditions within the Equatorial Zone (EZ). In this context, the EZ refers to Jupiter's equatorial region, encompassing the two fast-rotating eastward zonal jets located north and south of the equator. Using the two-layer moist convective Rotating Shallow Water (2mcRSW) model (Zeitlin, 2018), we explore the interactions between ammonia-driven convective processes and large-scale atmospheric dynamics in Jupiter's equatorial region. Historically, early thermodynamic models of Jupiter's atmosphere predicted the existence of three primary cloud decks above the 8 bar level, composed of $NH_3$, $NH_4SH$, and $H_2O$, from highest to lowest altitudes (Lewis, 1969; Weidenschilling and Lewis, 1973). Jupiter's atmospheric zonal flows extend to a depth of approximately 4% of the planet's radius (Kaspi et al., 2020). The 2mcRSW model used in this study represents only the upper convective cloud layers, where ammonia condensation (as both solid and aqueous solution) plays a key role in Jupiter's atmosphere, a hydrogen–helium gas giant. For the ammonia-driven convective layers occurring at pressures below 1 bar, the model remains relatively shallow compared to Jupiter's equatorial length scale, making the shallow water model particularly effective for capturing the dynamics in this region. In some shallow atmospheric models, Jupiter's fluid circulations are typically resolved within the outermost weather layers, extending from the visible cloud deck to several bars, or even tens of bars below (e.g. Showman, 2007; Schneider and Liu, 2009; Young et al., 2019).

Moist convection plays a crucial role in driving large-scale atmospheric dynamics on Jupiter by providing significant kinetic energy (Gierasch et al., 2000; Ingersoll et al., 2000). This convective mechanism provides sufficient energy to sustain and drive atmospheric eddies. Observations of Jovian lightning further support the existence of vigorous moist convection within the planet's atmosphere (e.g. Gibbard et al., 1995; Yair et al., 1995; Banfield et al., 1998; Little et al., 1999; Gierasch et al., 2000). Juno's microwave radiometer (MWR) revealed latitudinal variability in ammonia concentration, with Jupiter's equatorial region (0° N to 5°N) systematically darker, indicating a high, vertically uniform ammonia abundance, while other latitudes show lower and more variable concentrations (Li et al., 2017; Mousis et al., 2019; Guillot et al., 2020a). Ammonia increases with depth, reaching equatorial levels only below 30 bar (Bolton et al., 2017; Li et al., 2017). Early studies estimated that the water abundance in Jupiter's atmosphere would not exceed approximately five times the solar value (Guillot, 1995). However, subsequent moist convective models demonstrated that convective storms could form even with water abundances as low as 0.2 times the solar value (Hueso and Sánchez-Lavega, 2001). More recently, moist simulations with Jupiter-DYNAMICO (Boissinot et al., 2024), assuming tropospheric water abundances of 3 and 5 solar abundances (SA), show improved agreement with Jupiter's observed dynamics, particularly the well-defined super-rotating equatorial jet and stable mid-latitude jets. The 3 SA case closely matches observed jet magnitudes, consistent with Juno's reported atmospheric water abundance of 3 ±2 SA (Li et al., 2020). Water vapor and ammonia, though less complex than some stratospheric species on Jupiter, have significantly higher molar masses than the predominant hydrogen–helium atmosphere, in contrast to Earth, where water vapor is lighter than nitrogen–oxygen (Atreya et al., 1999; Giles et al., 2021). This difference introduces the virtual-temperature effect, where the presence of these heavier gases increases the density of air parcels compared to a hydrogen–helium parcel, thereby influencing buoyancy (Li and Ingersoll, 2015; Li et al., 2017). It is essential to distinguish this from the latent-heating effect, which relates to thermal energy changes during phase transitions like condensation (Emanuel, 1994). While both processes are crucial to Jupiter's atmospheric dynamics, the virtual-temperature effect affects density

and buoyancy, whereas latent heating drives thermal and convective responses (Iñurrigarro et al., 2020). Additionally, the presence of disequilibrium species such as phosphine ($PH_3$) and carbon monoxide (CO) indicates complex atmospheric processes, reflecting vertical mixing and photochemical reactions that further influence the planet's atmospheric behavior (Wang et al., 2016; Grassi et al., 2020).

Numerical simulations suggest that deep convection on Jupiter is primarily triggered by water condensation occurring at pressure levels ranging from approximately 5 bar to 500 mbar (Del Genio and McGrattan, 1990; Hueso and Sánchez-Lavega, 2001). At the upper altitudes of these convective plumes, where the pressure is a few hundred millibars, condensates such as $NH_3$, $H_2S$, and water are likely to form. In contrast, at pressures exceeding 3 bar, water becomes the dominant condensate (Banfield et al., 1998; Gierasch et al., 2000). Global climate model (GCM) simulations using Jupiter-DYNAMICO indicate weaker convective activity in the equatorial regions compared to mid- to high latitudes, consistent with lightning observations (Boissinot et al., 2024). It is also possible that during strong storms on Jupiter, ammonia vapor dissolves into lofted water ice at pressures between 1.1 and 1.5 bar, forming a low-temperature liquid mixture of ammonia and water. This process facilitates the formation of ammonia-rich *mushballs* that transport ammonia to deeper layers of the atmosphere (Becker et al., 2020; Guillot et al., 2020b).

Jupiter's Equatorial Zone (EZ) is characterized by robust zonal jets situated at the interfaces between its alternating dark and bright latitudinal bands, known respectively as belts and zones, with zonal speeds differing by up to 100 m/s (Tollefson et al., 2017). These jets form a prominent feature of Jupiter's atmospheric dynamics, with at least six alternating east–west zonal jet streams observable in each hemisphere (Ingersoll, 1990; Porco et al., 2003). The zonal wind profile within the EZ has been extensively documented, revealing dynamics that influence the broader atmospheric circulation (e.g. Limaye, 1986; García-Melendo and Sánchez-Lavega, 2001; Porco et al., 2003; Barrado-Izagirre et al., 2013). The zonal wind profile on Jupiter exhibits significant variation with depth. Data from the Juno mission revealed that the zonal jets extend down to depths of approximately 3000 km below the cloud tops (Kaspi et al., 2018; Read, 2024), although this interpretation has been challenged by Kong et al. (2018). Overall, the zonal winds gradually decay with increasing depth (despite possible enhancement in the outermost layers, as measured by the Galileo probe), largely due to the fluid's compressibility (Kaspi et al., 2009), increasing atmospheric density, and potential effects of Ohmic dissipation at these depths, where electrical conductivity begins to rise significantly (around 1 S/m) (Liu et al., 2008). This dissipation is linked to the planet's magnetic field and is believed to contribute to the damping of zonal flows at greater depths (Liu et al., 2008). The zonal winds show less variation at shallow depths, where they remain strong, especially in the equatorial region, but the jets become weaker with depth as the flows are constrained by the planetary magnetic field and internal dynamics. This depth corresponds to where Jupiter's observed cloud-level flows transition into deeper atmospheric layers (Kaspi et al., 2018, 2020). Duer et al. (2020) investigate a broad spectrum of possible interior zonal flow profiles, both latitudinally and vertically. Their findings indicate that, while deviations from the cloud-level zonal wind structure are theoretically possible, significant departures from the observed cloud-level flow are statistically improbable.

The EZ has been the site of several extreme episodes of cloud-clearing and 5-μm brightening at the equator, tracking the evolution of a cloud-free band south of the equator and the emergence of narrow, bright festoons from the hot spots (Antuñano et al., 2018). According to Antuñano et al. (2018), these disturbances lasted from 1 to 1.5 years, with formation timescales of under one month and dissipation timescales of less than four months. The southern hemisphere displays distinct cloud morphology; for example, in the vicinity of ≈ 7.5°S, a strong southern equatorial jet is accompanied by small,

periodic chevron-like features with unique cloud morphologies (Simon-Miller et al., 2012). These disturbances include repetitive chevron-shaped dark spots and transient large anticyclonic systems, collectively referred to as the South Equatorial Disturbance (SED) (Sánchez-Lavega and Montero, 1985). The observed differences in cloud morphology between the northern and southern EZ during these disturbances may be attributed to ammonia asymmetry, which is elevated in the EZ(N) compared to the EZ(S) (Achterberg et al., 2006; de Pater et al., 2016; Fletcher et al., 2016; Li et al., 2017). This supports the notion that plumes, festoons, and hot spots are connected to a Rossby wave in the NEB, where ammonia uplift feeds the cloudy and 5-μm-dark plumes, while subsidence depletes aerosols and gases from the hot spots and festoons (Cosentino et al., 2017; de Pater et al., 2016; Fletcher et al., 2016). During disturbances, the wave pattern extends southward through the equator, influencing the disturbed EZ(S) between 1° and 5°S at both cloud and 1–4 bar levels. This suggests that the wave pattern may be consistently present across the EZ, potentially obscured by thick ammonia clouds at higher altitudes until an EZ disturbance occurs or intensifying during such events (Antuñano et al., 2018).

Indeed, the present study investigates the dynamics of Y-shaped structures in Jupiter's EZ. Legarreta et al. (2016) identified two Y-shaped cloud formations in the EZ, which moved eastward at 20–40 m/s and persisted for 60–90 days. These features were shallow, located between the upper equatorial hazes and the main cloud deck. Through numerical simulations using shallow water models, they suggested that the structures were driven by Kelvin and Rossby waves, akin to Earth's equatorial dynamics. However, our findings reveal a different dynamical mechanism in the EZ. Large-scale, localized ammonia convection in Jupiter's upper layers generates a self-propagating and self-sustaining Y-shaped structure, referred to as a *hybrid* formation. This *hybrid structure* consists of an eastward-propagating quasi-barotropic coherent dipole coupled with a baroclinic Kelvin wave exhibiting a higher phase speed. The persistence of this coupling extends across inter-seasonal to seasonal timescales.

The structure of this manuscript is as follows: Section 2 provides a detailed description of the 2mcRSW model, including its assumptions, governing equations, linear wave spectrum, and boundary conditions, with an emphasis on its applicability to Jupiter's equatorial atmosphere. Section 3 presents a linear stability analysis, identifying conditions under which synoptic-scale disturbances in the Equatorial Zone (EZ) can grow, and exploring parameters such as atmospheric vertical structure, zonal jet strength, and stability diagrams. Building on the linear analysis, Section 4 examines the nonlinear evolution of identified instabilities through numerical simulations, showing how these disturbances develop and contribute to the formation of large-scale features in Jupiter's atmosphere. The interaction between moist convection and zonal jets is identified as a key driver of the observed dynamics. The results are contextualized within the broader framework of Jupiter's atmospheric dynamics, comparing findings with observational data and previous theoretical studies. We also discuss the implications for understanding equatorial disturbances on Jupiter, address the limitations of the current model, and suggest potential future research directions. Finally, Section 5 summarizes the main findings, emphasizing the results of linear stability analysis, the role of moist convection in the nonlinear evolution of the most unstable mode, and synoptic-scale Y-shaped disturbances in Jupiter's EZ.

## 2. The 2mcRSW model and its linear wave spectrum

In this study, we utilize two thin upper atmospheric layers within the framework of the 2mcRSW model. Historically, Rotating Shallow Water (RSW) models have been employed to investigate various aspects of Jupiter's atmosphere across multiple contexts (Dowling, 1994). For instance, the dynamics of solitary vortices have been examined in earlier works (Williams and Yamagata, 1984; Williams and Wilson, 1988), while Dowling and Ingersoll (1989) developed a two-layer

model specifically to analyze the Great Red Spot, assuming that the motions in the deeper layers are predominantly zonal and steady. Additionally, Thomson (2020) explored the influence of deep jets on Jupiter's weather layer using a 1.5-layer RSW model. More recently, the impacts of polar moist convective events on Jupiter's atmosphere have been studied with a single-layer RSW model (Hyder et al., 2022).

Layer models and level models represent two distinct methods for capturing the vertical structure of the atmosphere and oceans. Level models, which integrate thermodynamics easily, often exhibit reduced accuracy, especially in cases involving strong vertical gradients or rapid evolution of dynamics at high vertical modes. This is primarily due to their continuous density stratification and fixed depth finite differencing, which can lead to inaccuracies in such scenarios (Ripa, 1993). In contrast, layer models employ a piecewise constant density profile, allowing for the variation of interface depths with both position and time, thus enhancing accuracy at finer scales. This approach ensures the maintenance of a physically valid stratification, which is crucial for accurately representing the equations of motion. A prominent example of this distinction is found in the Laplace tidal equations (Proudman, 1942; Cartwright, 1978), which can be effectively modeled using a one-layer rotating shallow water (RSW) model, but do not have an equivalent level model representation (Ripa, 1993).

We emphasize that the simplified 2mcRSW model adheres to a minimal parameterization philosophy, capturing the full nonlinearity of hydrodynamic processes and the essential features of moist baroclinic instability development (Lambaerts et al., 2012). However, the 2mcRSW model in this study not only does not represent the entire depth of Jupiter's atmosphere but also simplifies the vertical structure of fluids by assuming only two layers with a sharp interface, neglecting gradual density transitions and vertical mixing. This limits its ability to capture the full complexity of internal waves, higher-order baroclinic modes, and vertical shear, as internal waves typically propagate through continuously stratified fluids and do not adequately respond to vertically propagating oscillations (see also Lindzen et al., 1968). In contrast, more complex models, such as Jupiter-DYNAMICO, range from a bottom pressure level of 10 bar at the base to 9 mbar at the top, while the thermal plume model successfully captures subgrid-scale convection (Boissinot et al., 2024). Another model capable of simulating the formation of moist convective storms from water condensation at deep pressure levels is the Explicit Planetary hybrid-Isentropic Coordinate (EPIC) General Circulation Model (GCM) (Sankar and Palotai, 2022). This model solves the primitive equations on an oblate spheroid (Dowling et al., 1998, 2006) using a hybrid vertical coordinate system (Konor and Arakawa, 1997) and incorporates bulk cloud microphysics parameterization (Palotai and Dowling, 2008).

The numerical scheme of the 2mcRSW model employed in this study is based on Bouchut (2007), utilizing a well-balanced, second-order finite volume approach for a two-dimensional shallow water model that accounts for Coriolis forces, topographic effects, and source/sink terms. This scheme accurately resolves inertia-gravity waves, including the formation of fronts (shocks) and precipitation boundaries, while maintaining balanced states. Key physical and mathematical features of the model – such as hyperbolicity, characteristic equations, finite relaxation time, front propagation and Rankine–Hugoniot conditions, the nature and speed of weak and strong discontinuities, parameter selection, and gravity current dynamics – have been investigated in both the one-layer model (Bouchut et al., 2009) and the two-layer version (Lambaerts et al., 2011b), including studies on internal wave scattering at stationary moisture fronts. This model has been frequently validated and used to investigate the instability of jets and vortices on Earth (e.g. Lambaerts et al., 2011a, 2012; Lahaye and Zeitlin, 2012a,b; Ribstein et al., 2014; Lahaye and Zeitlin, 2016; Gouzien et al., 2017; Rostami and Zeitlin, 2017, 2019a,b, 2020, 2022a,b) and on other planets, including investigations into Saturn's north polar hexagon (Rostami et al., 2017) and the evolution of Mars' annular polar vortex (Rostami et al., 2018). In recent years, an improved version of the mcRSW model
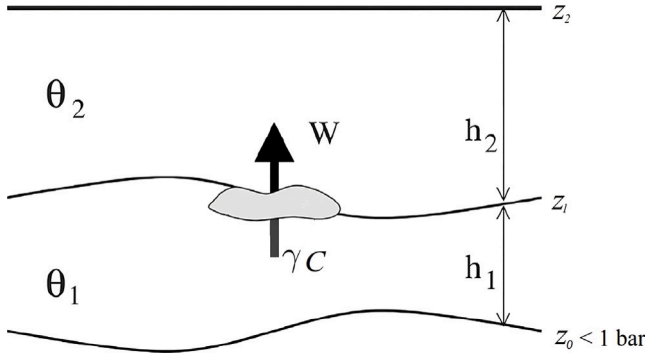
**Fig. 1.** Schematic of the two-layer moist-convective Rotating Shallow Water (2mcRSW) model, illustrating the ammonia-driven convective layer. This model captures the dynamics of ammonia condensation and convection within Jupiter's atmosphere, occurring at pressures below 1 bar.

has been developed, which, unlike classical RSW models, incorporates vaporization, temperature variation, and precipitable substances. This advancement has been thoroughly analyzed in terms of its conservation laws and general properties (Rostami and Zeitlin, 2018; Kurganov et al., 2020; Rostami et al., 2022, 2024b). The dynamical core of the moist-convective Thermal Rotating Shallow Water (mcTRSW) model has been implemented using a flux globalization-based, well-balanced, path-conservative central-upwind scheme (Cao et al., 2024) in a conceptual manner, and with pseudo-spectral spin-weighted spherical harmonics using the Dedalus (Vasil et al., 2019) algorithm in the Aeolus 2.0 atmosphere model, which has intermediate complexity (Rostami et al., 2024a).

The two-layer configuration of the 2mcRSW model was utilized in this study (Fig. 1). The 2mcRSW model is derived by vertically averaging the hydrostatic primitive equations, utilizing isobaric pseudo-height as the vertical coordinate (Hoskins and Bretherton, 1972). This approach allows for a self-consistent treatment of moisture, condensation, and the associated latent heat release by combining vertical averaging between isobaric surfaces with Lagrangian conservation of the linearized equivalent potential temperature (Lambaerts et al., 2011a). The governing equations of the 2mcRSW model describe a two-layer system, where the lower layer accounts for latent heat release from ammonia condensation. In contrast, the upper layer remains far from saturation and is characterized by a rigid lid at the upper material surface (Fig. 1). The equations are formulated as follows:

$$\partial_t \boldsymbol{v}_1 + (\boldsymbol{v}_1 \cdot \boldsymbol{\nabla})\boldsymbol{v}_1 + f(y)\hat{\boldsymbol{z}} \times \boldsymbol{v}_1 = -g\boldsymbol{\nabla}(h_1 + h_2), \tag{2.1a}$$

$$\partial_t \boldsymbol{v}_2 + (\boldsymbol{v}_2 \cdot \boldsymbol{\nabla})\boldsymbol{v}_2 + f(y)\hat{\boldsymbol{z}} \times \boldsymbol{v}_2 = -g\boldsymbol{\nabla}(h_1 + sh_2) + \underline{\frac{\boldsymbol{v}_1 - \boldsymbol{v}_2}{h_2}\gamma C}, \tag{2.1b}$$

$$\partial_t h_1 + \boldsymbol{\nabla} \cdot (h_1 \boldsymbol{v}_1) = \underline{-\gamma C}, \tag{2.1c}$$

$$\partial_t h_2 + \boldsymbol{\nabla} \cdot (h_2 \boldsymbol{v}_2) = \underline{+\gamma C}, \tag{2.1d}$$

$$\partial_t Q + \boldsymbol{\nabla} \cdot (Q\boldsymbol{v}_1) = \underline{-C + E}, \tag{2.1e}$$

In these equations, $\boldsymbol{v}_i = (u_i, v_i)$ denotes the horizontal velocity field in layer $i = 1, 2$ (numbered from the bottom), while $f(y)$ is the Coriolis parameter, defined as $\beta y$ on the equatorial beta-plane. The unit vector $\hat{\boldsymbol{z}}$ represents the vertical direction, and $h_i$ are the layer thicknesses, with equilibrium values $H_i$. The stratification parameter $s = \theta_2/\theta_1 > 1$ describes the ratio of potential temperatures between the layers, with $g$ representing gravitational acceleration. Without the underlined terms, Eqs. (2.1) correspond to the standard non-dissipative two-layer shallow-water model as described in Zeitlin (2018), with an additional passive scalar $Q$, representing the bulk ammonia content in the lower layer. This scalar is conserved under dry conditions, meaning no diabatic processes are involved. The underlined terms introduce the

key processes of condensation and evaporation. The lowest material surface of the two-layer model (2mcRSW) is situated at approximately 1 bar (Fig. 1). In this context, the condensation term $C$ encapsulates the latent heat release ($\gamma C$) associated with ammonia phase transition. Positive values of $C$ enhance low-pressure anomalies within the condensing lower layer, resulting in localized warming. Conversely, this process induces high-pressure anomalies in the upper layer, translating to a cooling effect. While $C$ serves as a condensation sink, $E$ functions as the bulk source of the condensable substance, which, in this case, is ammonia, within the moisture Eq. (2.1e). This convective flux also leads to Rayleigh drag in Eq. (2.1b), whose distribution across layers is not uniquely defined, as discussed in Rostami and Zeitlin (2018). In this study, we use the simplified formulation by Lambaerts et al. (2011a), which, when $h_2 \gg h_1$, reduces to the single-layer mcRSW model introduced in the Introduction. The condensation process is parameterized using a relaxation method, where the condensation rate $C$ is defined as:

$$C = \frac{Q - Q^s}{\tau}\mathcal{H}(Q - Q^s), \tag{2.2}$$

where $\mathcal{H}$ is the Heaviside step function. $E$ is modeled by the bulk formula:

$$E = \alpha\frac{|\boldsymbol{v}_1|}{|\boldsymbol{v}_{max}|}(Q^s - Q)\mathcal{H}(Q^s - Q), \tag{2.3}$$

where $|\boldsymbol{v}_{max}|$ represents the maximum velocity in the lower layer, and $\alpha$ is an adjustable coefficient. The condensation parameterization in (2.2) follows the Betts–Miller type (Betts and Miller, 1986), commonly used in general circulation models, while the evaporation parameterization in (2.3) is standard for ocean–atmosphere exchanges (Katsaros, 2001), with a normalization by the maximum velocity for simplicity. Notably, the term $E$ in the model functions exclusively as a source of condensable substance; even when adopting the formulation ($Q^s - Q)\mathcal{H}(Q^s - Q)$ with an initial uniform distribution of ammonia, the qualitative characteristics of the moist-convective outcomes remain similar. Ammonia is treated as a tracer field, facilitating the application of Betts–Miller type schemes that utilize analogous principles of latent heat release and phase change found on Earth. The fundamental physics of condensation applies to both environments, despite the differing condensates (ammonia versus water vapor). In a diabatic environment, condensation $C$ in the 2mcRSW model primarily occurs in convergent zones, as elaborated in the linear long-wave spectrum discussed in Appendix A. Conversely, when the condensable substance is the primary gas, such as carbon dioxide deposition on Mars, condensation takes place at locations where pressure exceeds a threshold necessary for deposition (cf. Rostami et al., 2018). The saturation value $Q^s$ is typically pressure-dependent, following the Clausius–Clapeyron relation, though it is assumed constant in this study for simplicity, as described in Bouchut et al. (2009). Additional processes, such as momentum dissipation due to bottom-layer friction, could be incorporated, and more complex boundary layer parameterizations are available, as in Schecter and Dunkerton (2009). However, these are omitted to maintain the model's simplicity. Radiative relaxation could also be included but is not considered in this study to focus on moist convection's role in driving atmospheric dynamics.

We select a scale height, defined as the height over which atmospheric pressure decreases by a factor of $e$, of $H_0 = 27,000$ m, representing the ammonia-driven convective layer. A scale height of 27 km in Jupiter's atmosphere, defined by $H_0 = R \cdot \mathcal{T}/g$, where $R$ is the specific gas constant, corresponds to a temperature ($\mathcal{T}$) of approximately 179 K (or about $-100\,°\text{C}$), including the convection and condensation of ammonia in the upper atmosphere. It is noteworthy that water vapor condenses into ice particles at approximately the 5-bar level, occurring about 50 km below the 1-bar level, while ammonia condensation occurs between 0.8 and 0.5 bar, and even as low as 0.2 bar in the EZ (Li et al., 2017; Guillot et al., 2020a). In the model setting, $\alpha = 0.15$, $Q^s = 0.88$, $Q_i = Q^s - 0.01$, and $\tau = 90\Delta t$, where

$\Delta t$ is the time step of the numerical scheme, selected to satisfy the CFL condition with $\Delta t = 10^{-3}T$, where $T = L_d/c$ represents the characteristic timescale (see also scale Eq. (3.1)).

Assuming adiabatic stable stratification of the consecutive layers, with material surfaces $z_0, z_1$, and $z_2$, we have:

$$\theta_{i+1} = \theta(z_i) + \frac{\mathcal{L}}{c_p}Q(z_i) \approx \theta_i + \frac{\mathcal{L}}{c_p} \tag{2.4}$$

Moist-convective fluxes are presented by vertical velocity $W$ through the upper boundary of the lower layer, expressed as $W = \gamma C$, where $\gamma = \mathcal{L}/\left[c_p\left(\theta_{i+1}-\theta_i\right)\right] \approx 1/Q(z_i) > 0$. In this context $\mathcal{L}$ denotes the latent heat of condensation and $c_p$ refers to the specific heat capacity of the condensable substance at constant pressure. The parameter $\gamma$ is set to 1 because it is incorporated into $\gamma C$ in the 2mcRSW model, allowing it to be absorbed into the timescale parameter $\tau$.

The conservation laws of the standard RSW model are modified in the presence of condensation and related convection. Although mass and bulk humidity are not conserved in the lower layer, their combination, defined as $m_1 = (h_1 - \gamma Q) > 0$, corresponds to the moist enthalpy in this simplified model and is locally conserved in the absence of evaporation $E$:

$$\partial_t m_1 + \nabla \cdot (m_1 \boldsymbol{v}_1) = 0. \tag{2.5}$$

This demonstrates the consistency of the model despite its simplicity. The potential vorticity (PV) equations for each layer, in the presence of condensation and with no evaporation ($E = 0$), are given by:

$$(\partial_t + \boldsymbol{v}_1 \cdot \nabla)q_1 = q_1 \frac{\gamma C}{h_1}, \tag{2.6}$$

$$(\partial_t + \boldsymbol{v}_2 \cdot \nabla)q_2 = -q_2 \frac{\gamma C}{h_2} + \frac{\hat{\boldsymbol{z}}}{h_2} \cdot \left[\nabla \times \left(\frac{\boldsymbol{v}_1 - \boldsymbol{v}_2}{h_2}\gamma C\right)\right]. \tag{2.7}$$

Here, $\zeta_i = \hat{\boldsymbol{z}} \cdot (\nabla \times \boldsymbol{v}_i) = \partial_x v_i - \partial_y u_i$ $(i = 1, 2)$ represents the relative vorticity, while $q_i = (\zeta_i + f)/h_i$ denotes the PV for each layer. Consequently, the PV in each layer is not a Lagrangian invariant in regions experiencing precipitation. In the absence of evaporation, the conservation of moist enthalpy in the lower layer allows us to derive a new Lagrangian invariant, specifically the moist PV:

$$(\partial_t + \boldsymbol{v}_1 \cdot \nabla)\frac{\zeta_1 + f}{m_1} = 0. \tag{2.8}$$

It is important to note that evaporation induces forcing in the system, thereby disrupting the conservation of moist enthalpy and moist PV. Caution should be exercised in numerical simulations that include evaporation, as the moist enthalpy must remain positive throughout to ensure thermodynamic stability. The dry energy of the system is given by:

$$\mathcal{E} = \iint dx\,dy\,(e_1 + e_2), \tag{2.9}$$

where the energy densities of the layers are defined as:

$$e_1 = \frac{1}{2}h_1 v_1^2 + \frac{1}{2}gh_1^2, \tag{2.10}$$

$$e_2 = \frac{1}{2}h_2 v_2^2 + gh_1 h_2 + \frac{1}{2}sgh_2^2. \tag{2.11}$$

Assuming no energy exchanges occur through the boundaries, we obtain:

$$\partial_t \mathcal{E} = -\int \gamma C \left[gh_2(1-s) + \frac{1}{2}(\boldsymbol{v}_1 - \boldsymbol{v}_2)^2\right] dx\,dy. \tag{2.12}$$

The first term in this equation corresponds to the generation of potential energy (for stable stratifications) due to upward convective fluxes, while the second term reflects the dissipation of kinetic energy due to Rayleigh drag. Although the horizontal momentum of individual layers is not conserved due to convective mass exchanges, the total momentum of the two-layer system remains conserved. Fig. 2 compares the left-hand side (LHS) and right-hand side (RHS) of Eq. (2.12). The LHS represents the numerically computed variation in total energy,
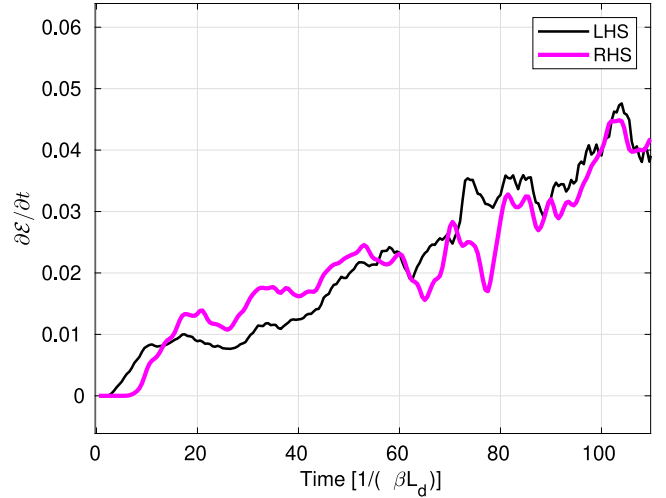


**Fig. 2.** Rate of change of total energy (Eq. (2.12)) in a moist-convective environment, with the black line representing the LHS and the magenta line the RHS of the equation, showing the evolution of the most unstable mode (see Sections 3 and 4).

accounting for the effects of evaporation, while the RHS corresponds to the theoretical prediction that excludes evaporation. This analysis pertains to the simulation of the instability evolution associated with the most unstable mode (see Fig. 5) in a moist-convective environment. Notably, the evaporation source term $E$ influences both the conservation laws and the total energy. In the absence of evaporation, moist enthalpy in the lower layer remains conserved, whereas with evaporation present, moist enthalpy is directly affected:

$$\partial_t m_1 + \nabla \cdot (m_1 \boldsymbol{v}_1) = -\gamma E, \quad m_1 > 0. \tag{2.13}$$

The mean water vapor content in the fluid column, $Q/h_1$, is similarly affected by the evaporation source $E$:

$$(\partial_t + \boldsymbol{v}_1 \cdot \nabla)\frac{Q}{h_1} = -\frac{m_1}{h_1^2} + \frac{E}{h_1}. \tag{2.14}$$

In this context, the moist potential vorticity (PV) is also not Lagrangian-invariant due to the source term from evaporation:

$$(\partial_t + \boldsymbol{v}_1 \cdot \nabla)\frac{\zeta_1 + f}{m_1} = -\frac{\zeta_1 + f}{m_1^2}\gamma E. \tag{2.15}$$

## 3. Linear stability analysis: Barotropic and baroclinic results

We introduce the unperturbed thicknesses of the layers, denoted by $H_i$ for $i = 1, 2$, and the unperturbed total thickness, which corresponds to the scale height, $H_0 = H_1(y) + H_2(y)$. The following scaling relations are applied to the independent and dependent variables in the *dry* version of the model:

$$(x, y) \sim L_d \equiv \frac{(gH_0)^{1/4}}{\beta^{1/2}}, \quad t \sim (\beta L_d)^{-1},$$

$$(u, v) \sim \beta L_d^2 \left(= \sqrt{gH_0} = c\right), \quad (h, b) \sim H_0, \tag{3.1}$$

where $L_d$ represents the horizontal length scale. In the model configuration, $L_d \approx 12,747\,\text{km}$, which corresponds to a latitude change of approximately $10.45°$ from the equator, $c = \sqrt{gH_0} \approx 818\,ms^{-1}$, and $T \approx 4\,\text{h}\,32\,\text{m}$. The region on Jupiter where the Coriolis parameter $f_0$ is smaller than the $\beta$ parameter exists at latitudes where $|\phi| < 20°$, which is also the region characterized by nearly liner variation in the $\beta$ parameter with respect to $y$. The dimensionless *dry* equations on the $\beta$-plane are given by:

$$\partial_t u_i + u_i \partial_x u_i + v_i \partial_y u_i - y v_i = -\partial_x(h_1 + s^{i-1}h_2), \tag{3.2a}$$

$$\partial_t v_i + u_i \partial_x v_i + v_i \partial_y v_i + y u_i = -\partial_y(h_1 + s^{i-1}h_2), \tag{3.2b}$$

$$\partial_t h_i + \partial_x \left[h_i - (2-i)b\right]u_i + \partial_y\left[h_i - (2-i)b\right]v_i = 0, \quad i = 1,2. \tag{3.2c}$$

It is evident that, in the absence of nontrivial topography (i.e., $b = $ const), any zonal jet with $u_i = U_i(y)$, $h_i = H_i(y)$, $v_i = 0$ represents a stationary solution. Observational data indicate that zonal flows are approximately in geostrophic balance, associated with latitudinal temperature variations between zones and belts, where zones are typically warmer than belts (Ingersoll and Cuzzi, 1969). It is important to note that the ridges and troughs associated with Jupiter's deeper abyssal jets represent nontrivial dynamic topography, which has a first-order effect on Jupiter's tropospheric dynamics. This influence is exerted through the stretching vorticity in the potential vorticity field (Read, 2024). In geostrophic equilibrium, the relationship is given by:

$$yU_i = -\partial_y(H_1 + s^{i-1}H_2) \tag{3.3}$$

We derived analytical curve fits for the mean zonal winds, averaged from IOPW observations in 2011 (Barrado-Izagirre et al., 2013), to obtain the corresponding $H_i$ for each layer. An advantage of analytical curve fitting is its ability to filter out spurious eigenmodes. The latitudinal extent of zone/belt boundaries can vary, occasionally receding or extending beyond the jet cores (Simon et al., 1998). While our analytical curves are symmetric about the equator, most observational studies report slight asymmetries in zonal winds (cf. Limaye, 1986; Simon, 1999; Porco et al., 2003). We restrict the simulations to symmetric zonal winds to preserve an idealized configuration and reduce the emergence of Yanai and inertia-gravity wave instabilities associated with asymmetry. García-Melendo et al. (2011) analyzed Jupiter's equatorial region and found significant longitudinal variations in the 6°N eastward jet's intensity, reaching up to 60 m/s, observed in both Cassini and HST data. These variations were attributed to Rossby wave activity rather than vertical wind shears. Once this variability was accounted for, the equatorial jet exhibited a symmetric structure about the equator, with peaks ($\approx$140–150 m/s) at 6°N and 6°S at similar pressure levels, despite localized asymmetries at 6°N.

If $b = 0$, as will be considered below, we obtain non-zero velocities $U_1$ and $U_2$ with shear, such that the upper layer exhibits a larger amplitude than the lower one. Consistent with the traditional perspective (Hess and Panofsky, 1951; Ingersoll and Cuzzi, 1969), we assume that the amplitude of the deep atmosphere's zonal velocity is weaker than that of the upper layer (Fig. 7).

We introduce small perturbations to all variables, denoted by primes, relative to the upper and lower layer jets:

$$u_i = U_i(y) + u_i',$$
$$v_i = v_i',$$
$$h_i = H_i(y) + \eta_i',$$

and linearize the Eqs. (3.2) with $b \equiv 0$ about the stationary solution. Dropping the primes, we obtain:

$$\partial_t u_i + U_i(y)\partial_x u_i + v_i \partial_y U_i(y) - yv_i + \partial_x(\eta_1 + s^{i-1}\eta_2) = 0, \tag{3.4a}$$

$$\partial_t v_i + U_i(y)\partial_x v_i + yu_i + \partial_y(\eta_1 + s^{i-1}\eta_2) = 0, \tag{3.4b}$$

$$\partial_t \eta_i + U_i \partial_x \eta_i + H_i \partial_x u_i + v_i \partial_y H_i + H_i \partial_y v_i = 0. \tag{3.4c}$$

We seek harmonic solutions to (3.4) in the form:

$$(u_i, v_i, \eta_i) = \text{Re}\left[(\tilde{u}_i, i\tilde{v}_i, \tilde{\eta}_i)e^{i(kx-\omega t)}\right]$$

Complex eigenfrequencies $\omega = \omega_R + i\omega_I$ with a positive imaginary component ($\omega_I > 0$) correspond to instabilities characterized by a linear growth rate $\sigma = \omega_I$. The resulting eigenproblem is:

$$L\left[\tilde{u}_1 \ \tilde{v}_1 \ \tilde{\eta}_1 \ \tilde{u}_2 \ \tilde{v}_2 \ \tilde{\eta}_2\right]^{\text{T}} = \omega\left[\tilde{u}_1 \ \tilde{v}_1 \ \tilde{\eta}_1 \ \tilde{u}_2 \ \tilde{v}_2 \ \tilde{\eta}_2\right]^{\text{T}},$$

$$\left[\tilde{u}_1 \ \tilde{v}_1 \ \tilde{\eta}_1 \ \tilde{u}_2 \ \tilde{v}_2 \ \tilde{\eta}_2\right]^{\text{T}} \equiv \begin{bmatrix} \tilde{u}_1 \\ \tilde{v}_1 \\ \tilde{\eta}_1 \\ \tilde{u}_2 \\ \tilde{v}_2 \\ \tilde{\eta}_2 \end{bmatrix}, \tag{3.5}$$

$$L = \begin{bmatrix} kU_1(y) & U_1'(y) - y & k & 0 & 0 & k \\ -y & kU_1(y) & -D & 0 & 0 & -D \\ kH_1 & H_1'(y) + H_1(y)D & 0 & 0 & 0 & 0 \\ 0 & 0 & k & kU_2(y) & U_2'(y) - y & sk \\ 0 & 0 & -D & -y & kU_2(y) & -sD \\ 0 & 0 & 0 & kH_2(y) & H_2'(y) + H_2(y)D & kU_2(y) \end{bmatrix}, \tag{3.6}$$

where $D$ denotes the operator of differentiation with respect to $y$, which will be discretized as the Chebyshev differentiation matrix, and the prime denotes the derivative of the corresponding functions with respect to their argument $y$.

Fig. 3 illustrates the relationship between the zonally averaged velocity and the corresponding pressure anomalies, interpreted within a one-layer geostrophic balanced state. The pressure anomalies depicted are relative to a zonal mean state, with the best analytical curve fit representing a barotropic pressure anomaly deviated by approximately 6% from the rest state. The corresponding thickness variations $H(y)$ for each zonal velocity profile $U(y)$ are calculated using Eq. (3.3).

The analytical curves 1 and 2, depicted in Fig. 3 as the solid black and dashed red lines, represent the best fits of the background mean flow in the absence of disturbances. These curves are highly stable, exhibiting minimal changes even under slight perturbations. Although these curves fall within the margin of error, the other analytical curves have been intentionally exaggerated to investigate the effects of higher zonal winds on their linear instability growth rates. For the best-fit curves, linear instability growth corresponds to zonal wavenumbers 4 to 7. However, under stronger zonal winds, as shown in Fig. 3, the most unstable modes shift to lower wavenumbers, specifically 4 and 5, as shown in Fig. 4. The phase velocities of both the first and second unstable modes exhibit a descending trend up to zonal wavenumber 4, after which they ascend. Since the phase velocity shows a consistent behavior across the rows, it suggests a systematic behavior of the jet's dynamics as represented by the different analytical curves. Fig. 5 illustrates the pressure fields for the most unstable mode (left panel) and the second most unstable mode (right panel) on the equatorial $\beta$-plane, as determined from the barotropic configuration derived from the optimal Analytical Curve fit. The left panel depicts a symmetric pressure pattern similar to Rossby waves, featuring alternating high and low-pressure regions symmetrically aligned with the jet axis. In contrast, the right panel exhibits an asymmetric pressure field. The arrows in both panels represent the velocity fields, which clarify the dynamics of these unstable modes. The resemblance to Rossby waves emphasizes the underlying mechanisms driving these instabilities. To further investigate the most unstable mode and assess the consistency of these results for enhanced zonal jet velocities, we applied a similar stability analysis for Analytical Curve 4 (see Fig. 3) with higher resolution (see Fig. 6) for the barotropic structure. The analysis indicates that strong jet conditions also reveal the most unstable mode as Rossby waves, particularly near the latitude of the zonal jet.

Fig. 7 shows the zonally averaged velocities and corresponding pressure anomalies within a two-layer geostrophic balanced state. The upper layer exhibits higher velocity amplitudes and a positive pressure anomaly near the equator, while the lower layer shows a negative anomaly. These pressure anomalies, relative to a zonal mean state, are represented by the best analytical curve fit, highlighting a baroclinic pressure deviation from the rest state.
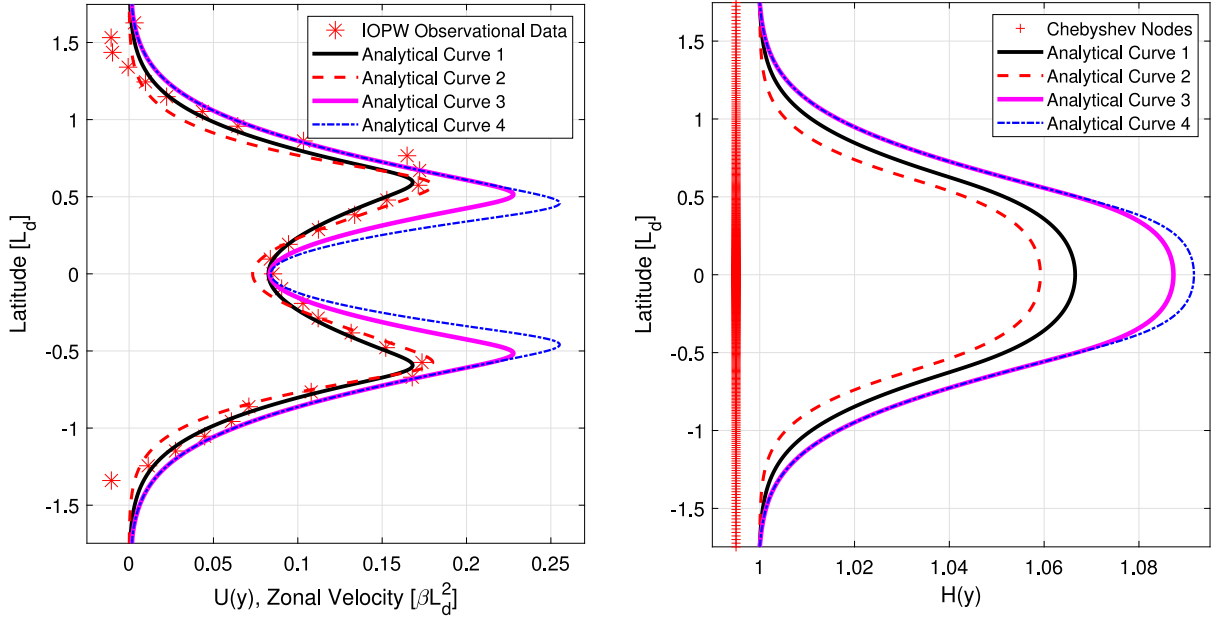
**Fig. 3.** Analytically defined profiles of zonal velocity $U(y)$ (left panel), based on the averaged mean zonal winds from IOPW observations in 2011 (Barrado-Izagirre et al., 2013), and the corresponding thickness deviations $H(y)$ with Chebyshev nodes (right panel), aligned with the analytic velocity profiles, are shown for a one-layer geostrophic balanced adjustment.

The stability diagrams for the baroclinic configuration (Fig. 8) reveal that the most unstable modes for the best-fit background mean flows correspond to zonal wavenumbers 4 to 6. However, as zonal velocities are increased, the most unstable mode shifts to a lower wavenumber, specifically $k = 4$. This indicates a sensitivity of the instability characteristics to the strength of the zonal wind. The stability diagrams for the baroclinic structures, where the mean zonal velocity in the lower layer is 70% of that in the upper layer, are presented in Fig. 8. Adding shear velocity to the system increases the growth rate of instability. In the baroclinic configuration, similar to the barotropic case, we observe a shift of the most unstable modes to lower wavenumbers under stronger disturbances, as shown in Fig. 8. A comparison between the barotropic and baroclinic stability diagrams highlights a notable difference: the phase velocity of the unstable modes in the baroclinic scenario is lower than in the barotropic case. Fig. 9 illustrates the geostrophic streamfunctions of the most unstable mode in the baroclinic scenario. Geostrophic streamfunctions from both barotropic and baroclinic linear stability analyses reveal a sequence of cyclonic and anticyclonic rotation patterns for the most unstable modes (Figs. 5 and 9). In the presence of diabatic processes, the cyclonic component is expected to become more intense during the nonlinear saturation of instability. Specifically, in the two-layer configuration, the intensification of cyclonic components in the lower layer is accompanied by a corresponding intensification of anticyclonic components in the upper layer, as discussed in Section 4.

Fig. 10 presents the dispersion relations of most equatorial waves corresponding to the best curve fit, highlighting their propagation characteristics across different dynamic regimes. These include barotropic and baroclinic Kelvin waves, which are eastward-propagating and non-dispersive, with the barotropic mode exhibiting a higher phase speed; Rossby waves, which typically propagate westward due to potential vorticity conservation; Mixed Rossby-Gravity (Yanai) waves, which combine characteristics of both Rossby and gravity waves; and Inertia-Gravity waves, influenced by the balance between Coriolis and pressure forces.

Fig. 11 presents the phase portraits of the geostrophic stream functions for the dominant low-frequency stable modes on the equatorial

$\beta$-plane, as derived from the optimal Analytical Curve fit (see Fig. 7). The figure depicts three distinct phase portraits of inertial gravity waves (IGWs). The first through third rows illustrate these IGWs at progressively lower frequencies, ranging from highest to lowest. Additionally, the fourth row showcases an off-equatorial Rossby wave, which is influenced by external shear forces.

On Jupiter, the phase portraits of baroclinic Kelvin waves (BCKWs) and Yanai waves exhibit distinctive dynamical structures that reflect the interplay between the planet's rapid rotation and its strongly stratified troposphere. The BCKWs, characterized by eastward propagation with minimal meridional displacement, typically exhibit phase lines that are nearly zonally aligned, indicative of a robust zonal jet and a non-dispersive wave nature with a high intrinsic phase speed. In contrast, Yanai waves, which represent a hybrid mode combining characteristics of both Rossby and inertia-gravity waves, display phase portraits with significant meridional curvature, resulting in a diagonal phase line orientation relative to the equator, highlighting the influence of the Coriolis effect and planetary vorticity gradients. In Fig. 12, these phase portraits are depicted for the dominant low-frequency stable modes on the equatorial $\beta$-plane, derived from the optimal Analytical Curve fit (refer to Fig. 7). The upper layer, represented by [$\psi_2 = \eta_1 + s\eta_2$], and the lower layer, represented by [$\psi_1 = \eta_1 + \eta_2$], facilitate the examination of wave dynamics across different stratified atmospheric layers. The top row illustrates the phase portrait of BCKWs, where the phase lines align predominantly along the zonal direction, consistent with their high Rossby number and fast wave speed. The bottom row displays the phase portrait of the Yanai wave, characterized by a more complex structure due to the coupling between Rossby wave dynamics and inertia-gravity wave propagation. Both wave modes are computed for a zonal wavenumber of $k = 4$, and the associated velocity field, indicated by vectors, elucidates the dynamical interactions within these stratified atmospheric layers.

## 4. Evolution of nonlinear instabilities in moist-convective flows

We initialize the model using the background zonal velocity field derived from the optimal Analytical Curve fit, which represents the
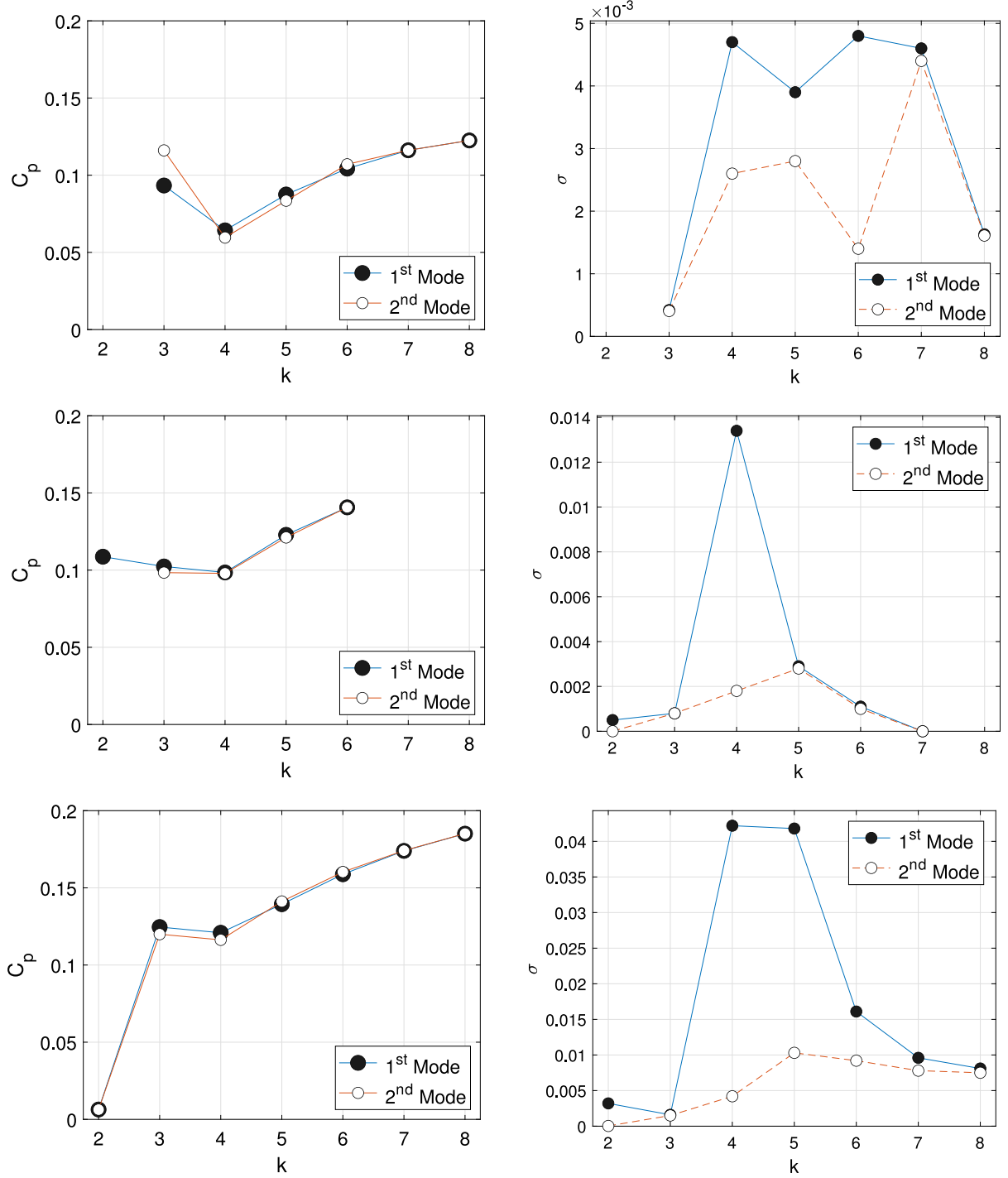
**Fig. 4.** Stability diagrams of the barotropic layer easterly jet corresponding to the analytical curves shown in Fig. 3 on the $\beta$-plane. The diagrams illustrate phase velocity (left panel) and growth rate (right panel) as functions of the zonal wavenumber $k$. The first and second unstable modes are indicated by black and white circles, respectively. The rows, from top to bottom, correspond to Analytical Curves 2 to 4. The $y$-axis range of the right panels is adjusted for better visibility. Analytical Curve 1 has not been shown due to its similarity to Analytical Curve 2 and negligible differences.

equilibrium state of Jupiter's atmosphere, and introduce a small perturbation in the form of the most unstable mode with a non-dimensional amplitude for wavenumber $k = 4$. This perturbation is designed to emulate the onset of instability within a stratified, rotating fluid under moist-convective conditions. Key results are summarized below:

(1) **Intensification of Cyclonic Vortices in the Convective Layer**
The results reveal the nonlinear amplification of the unstable mode, leading to the horizontal growth, elongation, and intensification of vortical structures. Specifically, the simulations show the formation of cyclonic vortices in the lower atmospheric layer
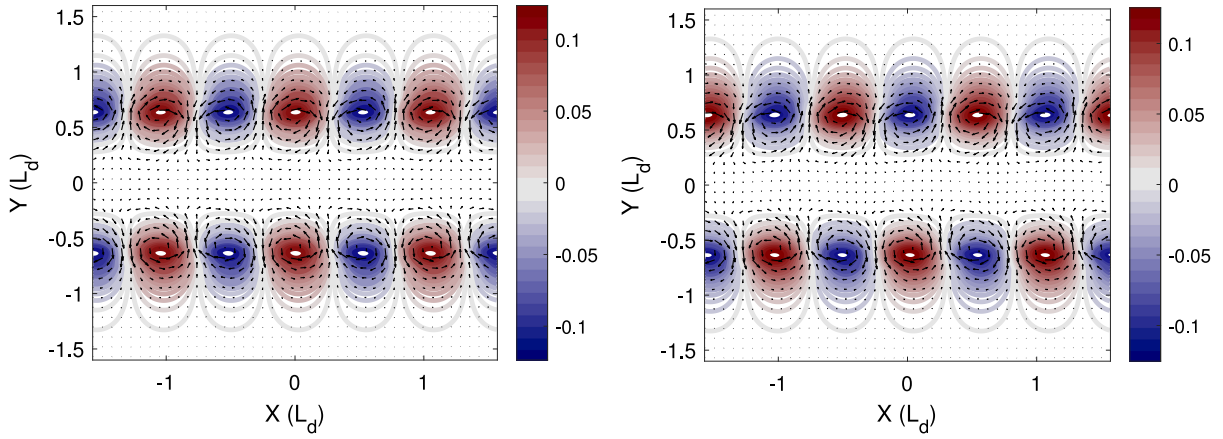
**Fig. 5.** Pressure fields for symmetric (left panel) and asymmetric (right panel) modes, corresponding to the barotropic configuration of the most unstable and second unstable modes on the equatorial $\beta$-plane, as derived from the optimal Analytical Curve fit. The color maps illustrate the pressure fields, while the arrows represent the velocity fields associated with these unstable modes.

and anticyclonic vortices in the upper layer, both driven by the release of latent heat through moist convection (Fig. 13).

The first signs of condensation, detectable at visual wavelengths, emerge within the simulation after a few Jovian days. This is consistent with the expected timescale for convective processes to significantly influence large-scale circulation patterns. As kinetic energy in the lower layer increases, a corresponding intensification of the upper layer vortices is observed, further reinforcing the critical role of moist convection as a primary mechanism for converting heat flow into kinetic energy in Jupiter's atmosphere (Gierasch et al., 2000). In this context, moist convection in Jupiter's atmosphere functions analogously to tropical storms on Earth, driving key circulations within Jovian vortices.

(2) **Belt Inhibition of Convective Vortices**

Fig. 13 illustrates the development of low-pressure anomalies in the convectively driven lower layer as the unstable mode intensifies, while anticyclonic ovals emerge in the upper layer. These convective vortices are located away from the latitude of the maximum zonal jet, specifically where $|y| > 0.7L_d$. The meridional extension of instabilities also predominantly occurs in these regions. The positioning of convective areas within the belts supports the argument of a net rising motion in these regions due to moist convection (Ingersoll et al., 2000). The patterns of condensation and vorticity (Fig. 14) closely resemble observational images, which also show an absence of similar convective storms in the bright zones (e.g., Porco et al., 2003). The presence of complex vorticity and the strong connection between visible cloud tops and Jupiter's convective interior has long been discussed in the literature (e.g., Smith et al., 1979; Ingersoll et al., 2000; Ingersoll, 2002). However, to the best of our knowledge, the nonlinear evolution of the most unstable mode-based on classical linear stability analysis relative to balanced zonal velocity—in an idealized shallow water moist-convective model has not been previously explored.

(3) **Patches of Synoptic and Mesoscale High White Cloud Clusters**

The condensation patterns in Fig. 14 reveal large-scale condensation regions on the order of $0.1\,L_d$, located at low latitudes on the poleward side of each eastward jet $|y| > 0.7L_d$. These patches are associated with upwelling and moist convection, which may also be influenced by vertical shear velocity. These localized areas manifest in Jupiter's atmosphere as lightning and high white cloud clusters. Such optically thick white cloud clusters have been observed in data from the Galileo spacecraft (Banfield et al., 1998; Little et al., 1999; Gierasch et al., 2000), as well as

in high-resolution narrow-angle photographs captured by Voyager 1 in February 1979 (Hueso and Sánchez-Lavega, 2001). Nevertheless, simulated convective activity is weaker in low-latitude regions compared to mid to high latitudes (Boissinot et al., 2024), as indicated by lightning observations. The Juno microwave radiometer has mapped the meridional distribution of lightning signatures associated with convective storms, revealing that these storms are both more intense and more frequent between latitudes of 30° and 70° relative to the equator (Brown et al., 2018).

(4) **Intensification of Shear Zonal Velocity During Active Convection**

The nonlinear evolution of instability in a moist-convective environment results in a significant intensification of shear zonal velocity. This intensification manifests as an eastward (upper layer) and westward (lower layer) acceleration outside the equatorial zone (EZ), specifically for latitudes $|y| > (0.75L_d \approx 7.5°)$, where $y$ represents the latitude (Fig. 15). Within the inner EZ, $|y| < 0.75L_d$, the zonal velocity intensification occurs in the opposite direction.

In the *dry* case, the zonal velocity intensification is two orders of magnitude smaller, rendering it negligible. For a quantitative perspective, assuming a scale height of $27\,\mathrm{km}$, the length scale $L_d$ is approximately 10.44°, and the velocity scale $\beta L_d^2$ is about $820\,\mathrm{ms}^{-1}$.

Fig. 15 illustrates that the nonlinear evolution of zonal velocity associated with the most unstable mode alters its sign at approximately $0.7L_d$ (around 7.3° Lat). These characteristics resemble the observed chevron-shaped oscillations, with an average chevron tip latitude of 7.5°S, although variability is observed among individual chevrons (Simon-Miller et al., 2012). Time series movies from Cassini images further demonstrate that the chevrons oscillate in latitude over both longitude and time (Simon-Miller et al., 2012).

Our linear stability analysis supports the explanation that the chevron-shaped patterns arise from the interaction between westward-propagating Rossby waves on the poleward side of the maximum zonal jet and eastward-propagating Kelvin waves, which dominate on the equatorward side between the two maximum zonal jets. The higher phase speed of the latter facilitates the formation of distinct chevron-shaped wave structures through their interacting dynamics. Additionally, Yanai waves and low- to mid-frequency inertio-gravity waves act as secondary unstable modes, influencing the equatorial zone between the two maximum zonal winds (see Figs. 11 and 12). The
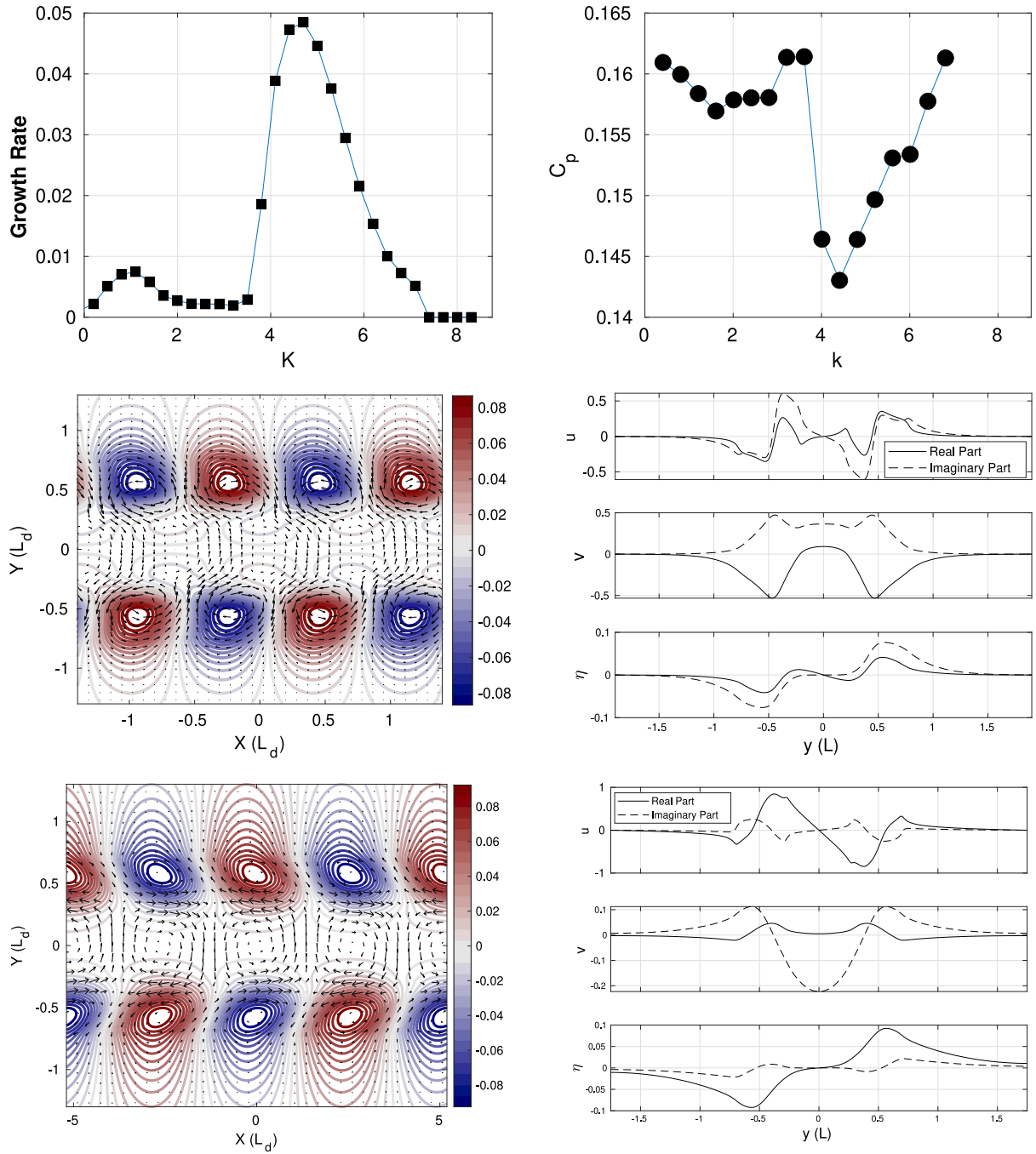
**Fig. 6.** Growth rates and phase speeds of the barotropic unstable modes as functions of the zonal wavenumber $k$ for curve 4 of the background flow (see Fig. 3). *Upper panels*: Growth rates and phase speeds as functions of $k$. *Middle panels*: Phase portrait of the most unstable mode at $k = 4.5$, highlighting its dominant characteristics and spatial structure. *Lower panels*: Phase portrait of the second peak unstable mode at $k = 1.2$, illustrating the phase alignment and features of the secondary instability.

nonlinear evolution (Fig. 14) further shows that the sign change of zonal velocity associated with the most unstable mode aligns with the latitudinal position of the most active sequence of relative vorticities.

(5) **Poleward Drift of the Emerged Instability**

In the absence of higher latitude jets, our simulations reveal a smooth meridional propagation of the emergent instability under diabatic conditions (Fig. 16). Observations of both Jupiter and Saturn provide little or no evidence of latitudinal drift in the extratropical zonal jets on decadal timescales (Read, 2024). Unlike observational studies, which show relatively stable zonal

jets in Jupiter's atmosphere, simulations often depict latitudinal migrations of zonal jets. These migrations, which were simulated under potentially diverse physical assumptions and numerical schemes, are characterized by either equatorward shifts (Williams, 2003; Young et al., 2019) or poleward displacements (Chemke and Kaspi, 2015). Poleward-drifting jets have also been observed in simulations of deep convection in spherical shells (e.g., Rotvig, 2007; Guervilly and Cardin, 2017). Similarly, some laboratory experiments incorporating a topographic $\beta$-effect have reproduced drifting jets (Smith et al., 2014), whereas jets formed in quasi-geostrophic models on a
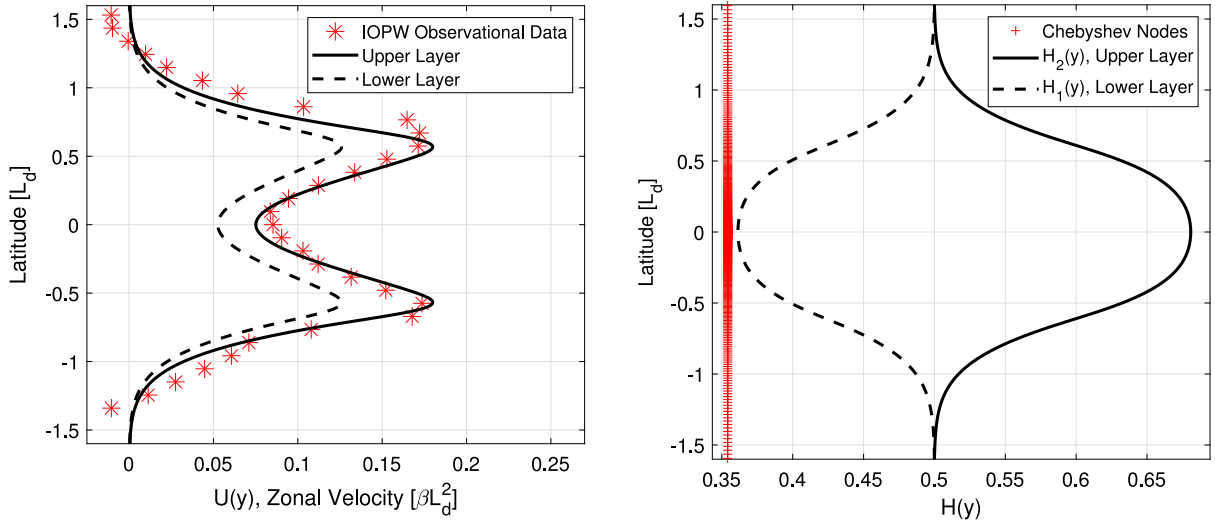
**Fig. 7.** Profiles of zonal velocity $U_i(y), i = 1, 2$ for the upper (solid line) and lower (dashed line) layers, with the upper layer corresponding to Analytical Curve 2 in Fig. 3 (left panel). The right panel shows the corresponding thickness deviations $H_1(y)$ and $H_2(y)$, along with Chebyshev nodes, based on the analytic velocity curves.

uniform $\beta$-plane did not exhibit the same drift behavior (Jones et al., 2003).

Our results suggest a strong coupling between the kinetic energy of upper-layer anticyclones and lower-layer cyclones. As the lower-layer cyclones tend to drift poleward, the upper-layer anticyclones follow. This is clearly depicted in Fig. 16, which shows the Hovmöller diagram of kinetic energy for the initialized perturbation along $X = 0$, revealing poleward drifts in both the lower (right panel) and upper (left panel) layers.

A key factor influencing the stationary, meandering, or drifting behavior of zonal jets is the variation in the background potential vorticity (PV) gradient across individual jets. For instance, Saturn's north polar vortex flattens the PV gradient within the hexagonal jet (Rostami et al., 2017). Indeed, the substantial variations in the effective background PV gradient with latitude, both on Jupiter and other similar planets, may hint at coupling with deep, stationary features such as tidal forces, which could anchor upper-level jets and prevent their drift (Tyler, 2022; Read, 2024). Thus, one possible explanation for the poleward drift of the zonal jets observed in this study is a limitation of the model, which does not include higher-latitude jets that could potentially influence the jet dynamics.

(6) **Co-location of Lightning, Convection, and Instability**

Galileo observations of lightning on Jupiter (Little et al., 1999) provide valuable insights into the dynamics of Jupiter's atmosphere. The images show that lightning storms in the equatorial region occur at latitudes approximately 5°–10°, which correspond to the latitudes of emerged instability and condensation in our simulation (e.g., Figs. 9, 14). This alignment supports the hypothesis that Jupiter's lightning tends to occur within the most unstable regions where the vorticity gradient changes sign. The Galileo images also confirm localized updrafts near Jovian lightning, reinforcing this connection. Additionally, studies based on Voyager 1 and 2 images indicate that barotropic stability is violated around 10° latitude (Ingersoll et al., 1981). Nevertheless, Jovian lightning predominantly occurs at higher latitudes rather than near the equator (Brown et al., 2018). This was confirmed through the detection of rapid whistlers and Jupiter-dispersed pulses, which were primarily observed at mid to high latitudes (Kolmašová et al., 2023).

The observed rarity of lightning in the southern hemisphere at equivalent latitudes, compared to our symmetric model configuration, may be attributed to an asymmetric distribution of condensates in the lower troposphere. Borucki and Williams (1986) reported that the origin of Voyager 1's flashes is at a depth of 5 bars, where water clouds are present. Numerical models of convective clouds suggest that this vertical extent could reach up to the 2-bar pressure level in the atmosphere (Yair et al., 1995). According to Juno's measurements of odd gravity harmonics (J3, J5, J7, J9), Jupiter's gravity field exhibits significant asymmetric features. These harmonics reveal a direct connection between the planet's north–south asymmetry and deep atmospheric flows, with J3 sensitive at depths below 3000 km and J5 constraining flows up to 3500 km. The findings indicate that this asymmetry arises from deep winds extending thousands of kilometers beneath the cloud layer, differing from surface observations, and that notable deviations in the meridional profile of zonal winds are unlikely to align with the gravity data (Duer et al., 2020). Our conceptual model does not estimate the lifetime of Jovian lightning storms, as it includes a continuous source of humidity in the lower layer that is not based on empirical data.

## 5. Dynamics of the equatorial Y-shaped structure

In this section, we present a novel explanation for the Y-shaped, eastward-propagating cloud structures observed between September and December 2012 in ground-based and Hubble Space Telescope (HST) images. These structures are aligned along the equator and are centered at latitudes between approximately 5° and 10°. They are vertically confined between the upper equatorial hazes and the main cloud deck (Legarreta et al., 2016). These Y-shaped clouds extend zonally for about 15° (approximately 18,000 km) and meridionally for around 5° (approximately 6,000 km), with an eastward propagation speed of 20–40 m/s relative to Jupiter's mean flow (Legarreta et al., 2016). Legarreta et al. (2016) performed numerical simulations with Gaussian disturbances initialized along the equator, which replicated the well-known Matsuno–Gill mechanism. This mechanism generates eastward-propagating Kelvin waves and westward-propagating Rossby waves. In the simulations using the one-layer RSW model by Legarreta et al. (2016), with or without background zonal flow, the resulting structure forms a disjointed configuration. The symmetric lobes of the Rossby waves propagate westward relative to the excitation source and detach from the initial structure, while the Kelvin waves continue to propagate eastward.
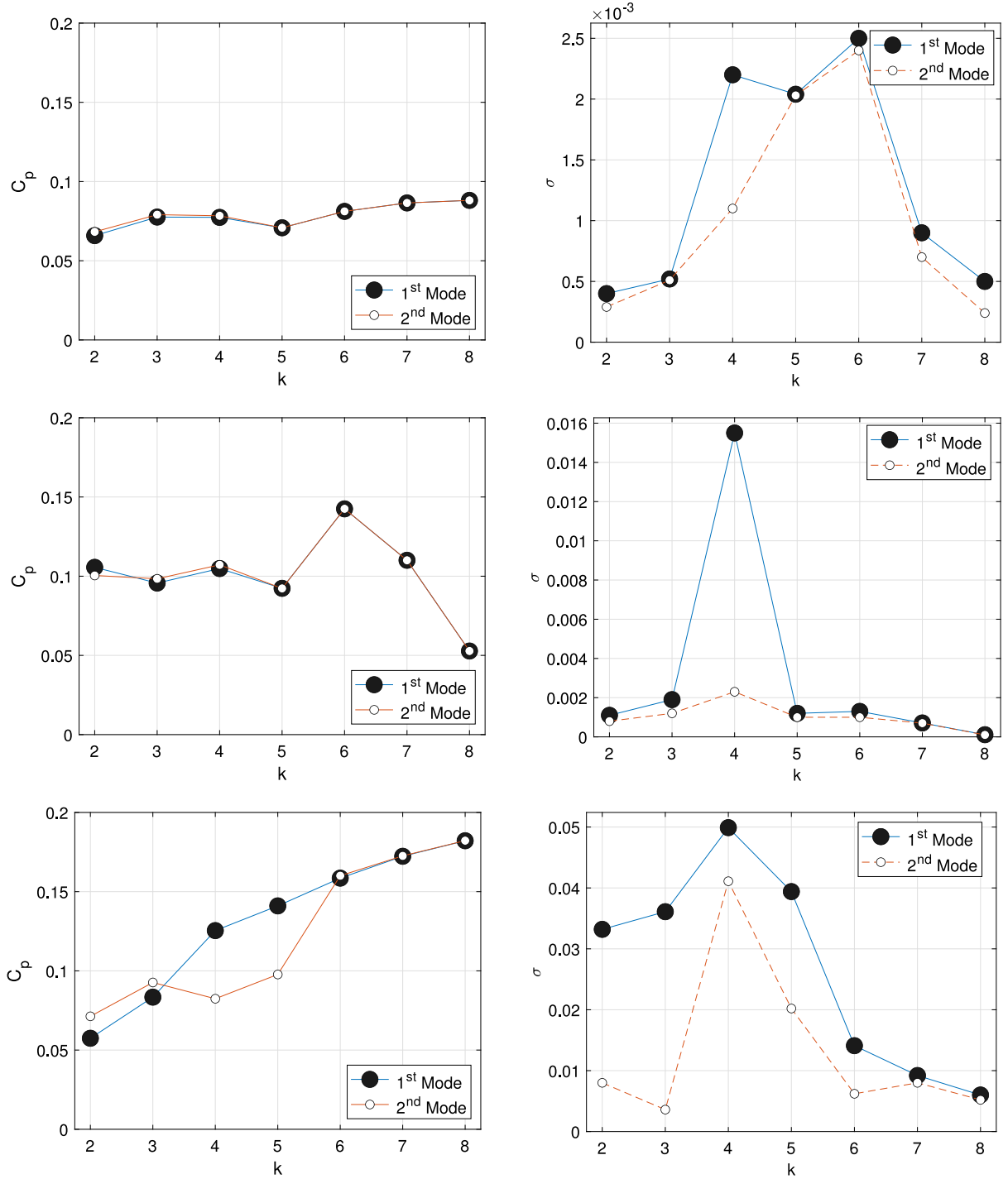
**Fig. 8.** Stability diagrams of the baroclinic easterly jet corresponding to the analytical curves shown in Fig. 7 on the $\beta$-plane, represented in terms of phase velocity (left panel) and growth rate (right panel) as functions of the zonal wavenumber $k$. The first and second unstable modes are indicated by black and white circles, respectively. The rows, from top to bottom, correspond to Analytical Curves 2 to 4. The $y$-axis range of the right panels is adjusted for better visibility. Analytical Curve 1 has not been shown due to its similarity to Analytical Curve 2 and negligible differences.

The alternative explanation in this study is grounded in recent advances in the understanding of Equatorial Modons and the localized adjustment of negative pressure anomalies in the lower troposphere over warm pools in moist convective environments (Rostami et al., 2022). A modon is defined as a form-preserving, uniformly translating, horizontally localized, nonlinear solution to the inviscid quasigeostrophic equations. Recent studies (Rostami and Zeitlin, 2019a,b, 2020, 2021; Zhao et al., 2021) have provided insights into equatorial systems that propagate slowly eastward, suggesting that these Y-shaped structures

may be generated in a self-sustained and self-propelled manner. This mechanism involves large-scale localized heating in the lower troposphere over warm pools, leading to the formation of a *hybrid structure*. This *hybrid structure* consists of a *baroclinic equatorial modon* coupled with a convectively driven, detaching baroclinic Kelvin wave that persists on an interseasonal timescale. A similar conceptual framework has been applied to understand Madden–Julian Oscillation (MJO)-like phenomena on Earth's equator, lending further support to our proposed mechanism (Rostami and Zeitlin, 2020; Rostami et al., 2022).
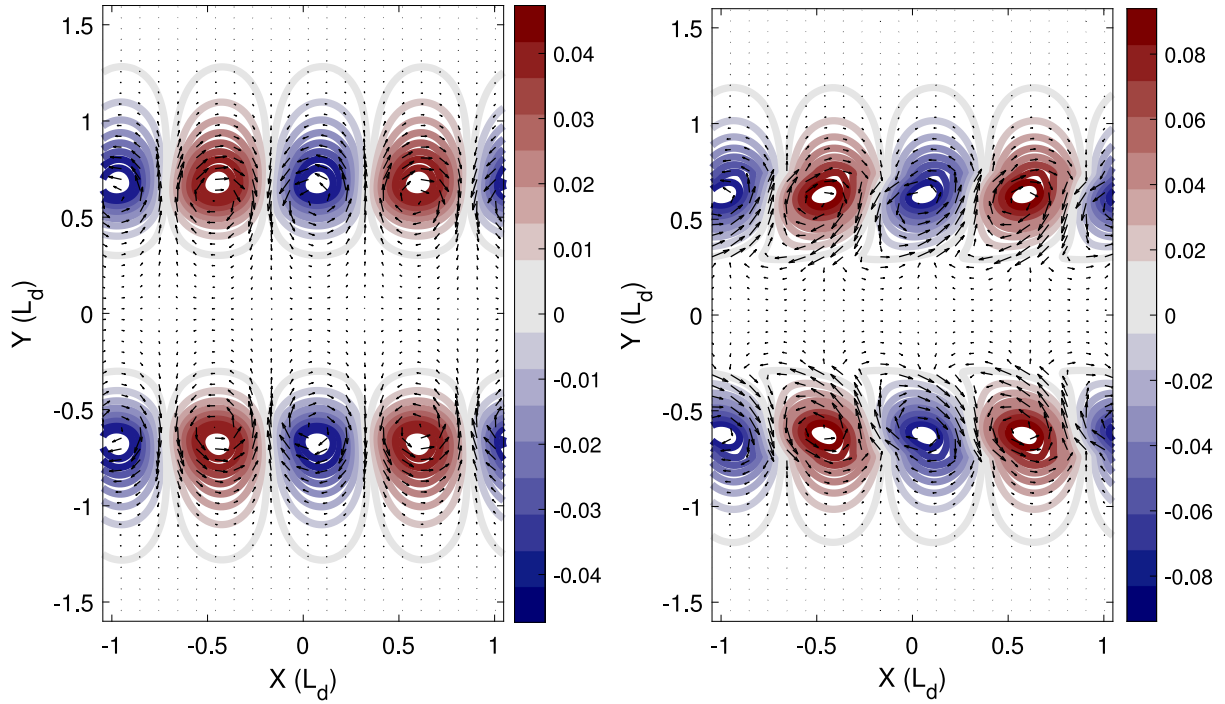
**Fig. 9.** Geostrophic streamfunctions of the most unstable mode on the equatorial $\beta$-plane, shown for the upper layer $[\psi_2 = \eta_1 + s\eta_2]$ (left panel) and the lower layer $[\psi_1 = \eta_1 + \eta_2]$ (right panel). The velocity field is represented by arrows.
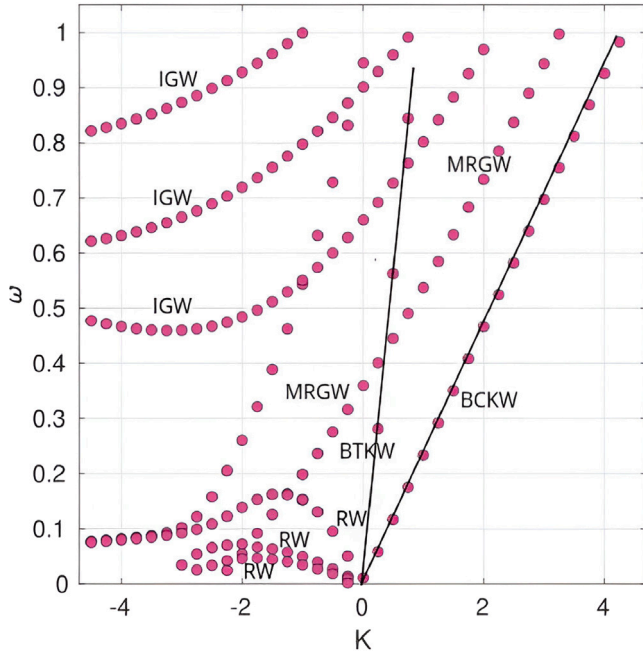


**Fig. 10.** Dispersion relations for configurations corresponding to the optimal Analytical Curve fit, illustrating the wave propagation characteristics across different dynamic regimes. The figure includes the following abbreviations: BTKW (Barotropic Kelvin Wave), BCKW (Baroclinic Kelvin Wave), MRGW (Mixed Rossby-Gravity or Yanai Wave), IGW (Inertia-Gravity Wave), and RW (Rossby Wave).

We introduce an equatorial disturbance as a negative pressure anomaly in the lower layer pressure field using an alpha-Gaussian profile. For details on the initialization of the equatorial disturbance in Jupiter's atmosphere, including parameter settings and profile specifics, please refer to Appendix B. Fig. 17 illustrates the equatorial adjustment

of a symmetric negative thickness anomaly, representing a pressure disturbance, in both *dry* and moist-convective environments without any background zonal velocity. An asymmetric perturbation would induce the emergence of Yanai waves as the system responds to the initial depression. At the onset of geostrophic adjustment, a quasi-isotropic inflow converges toward the equatorial center of the anomaly, with wind intrusion from extratropical regions observed in large-scale disturbances. The initial stages feature the emission of fast, short-wavelength inertia-gravity waves, followed by cyclonic circulation on both sides of the equator, driven by the Coriolis force. In moist-convective environments, these cyclones intensify, evolving into a quasi-equatorial modon. Subsequently, a weaker vorticity dipole of opposite sign emerges and attaches to the eastern edge of the primary dipole, forming a zonally asymmetrical quadrupole. Simultaneously, a weaker quadrupole of opposite sign develops in the upper layer, causing the entire system to gradually drift eastward. In cases of weaker moist convection, the cyclones propagate westward as Rossby waves. A key distinction between *dry* and moist-convective environments lies in the timing of the long-wave convectively coupled baroclinic Kelvin wave (CCBKW) detachment from the dipolar structure. In *dry* conditions, this detachment occurs much earlier, whereas in moist-convective settings, the detachment is delayed due to interseasonal variability, resulting in a Y-shaped equatorial structure. The *dry* case response aligns with Gill's mechanism (Gill, 1980), characterized by Rossby-wave emission to the west and Kelvin wave (KW) emission to the east of the localized anomaly. However, Fig. 17 also reveals a tipping point where an eastward-propagating dipolar structure emerges when the pressure anomaly reaches a critical threshold ($\Delta\eta_1/H \approx 0.07$) in moist-convective environments. Achieving a similar modon in a barotropic structure requires a greater pressure anomaly (Rostami and Zeitlin, 2019b), as latent heat release intensifies the self-sustained negative pressure anomaly. In weak convective scenarios, Gill's mechanism typically governs the response, leading to the transient formation of a Y-shaped pattern. In contrast, strong convective scenarios, characterized by significant low-pressure or high potential temperature anomalies, result in the development of a more persistent Y-shaped structure, consistent with the theory
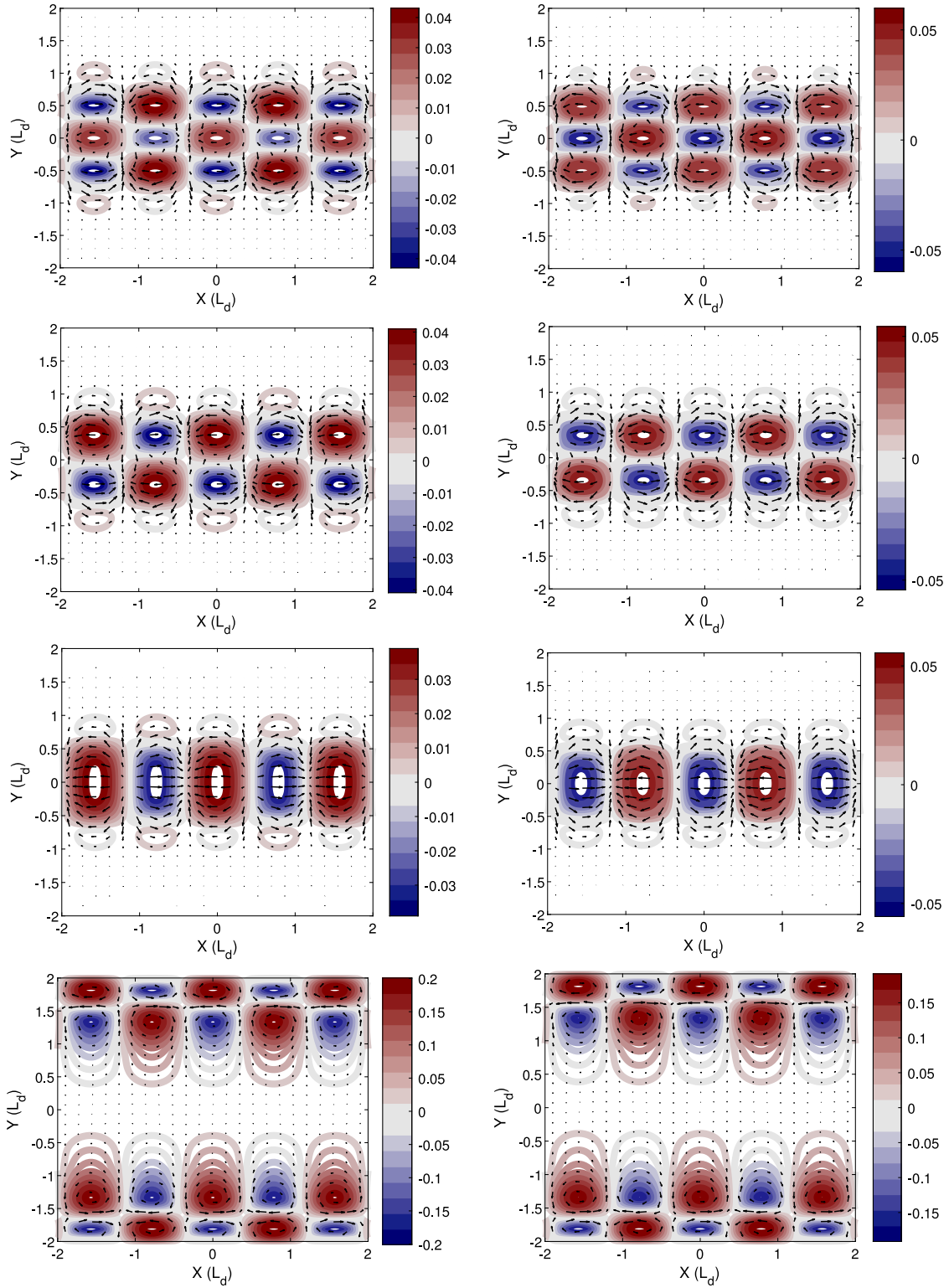
**Fig. 11.** Phase portrait of the geostrophic stream functions for the dominant low-frequency stable modes on the equatorial $\beta$-plane, corresponding to the optimal Analytical Curve fit (Fig. 7). The upper layer is represented by $\psi_2 = \eta_1 + s\eta_2$ (left panel) and the lower layer by $\psi_1 = \eta_1 + \eta_2$ (right panel). The velocity field is indicated by arrows. The displayed modes are inertial gravity waves (IGWs) for $k = -4$. The first through third rows depict these waves at the highest to lowest frequencies, respectively. The fourth row illustrates the off-equatorial Rossby wave influenced by the external shear.

of MJO-like patterns on Earth proposed by Rostami et al. (2022). Both transient and sustained Y-shaped configurations have been documented in observational studies (Rogers, 1995; Legarreta et al., 2016). The transition from Rossby waves to a dipolar or quasi-equatorial modon occurs early in the adjustment process, with baroclinic configurations

requiring a lower amplitude of pressure anomaly than barotropic structures (Rostami and Zeitlin, 2019a). The fusion of the dipole with the CCBKW, leading to the formation of a quadruple structure (Fig. 18), is a purely baroclinic effect. Condensation slows the CCBKW while enhancing the dipolar gyres, enabling eastward propagation akin to
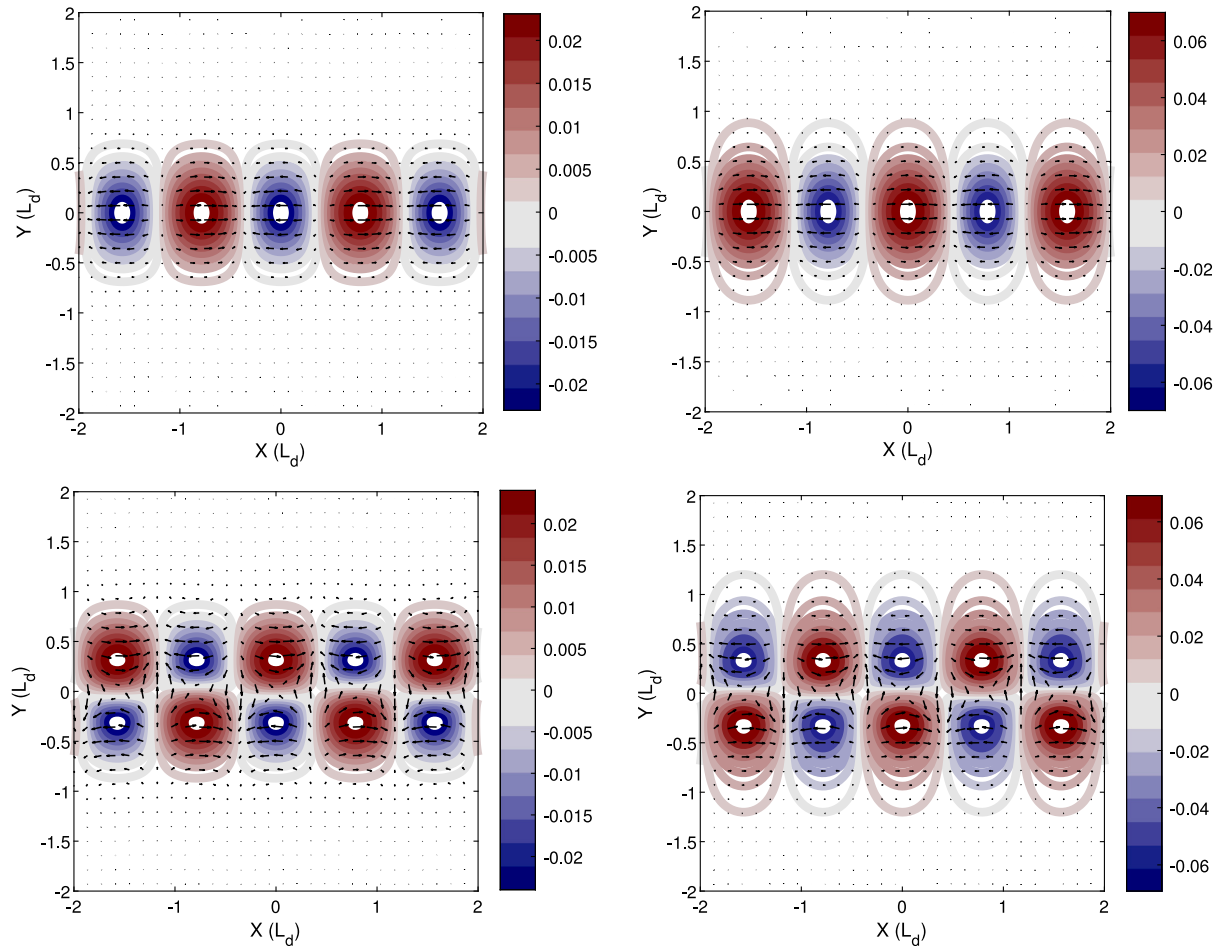
**Fig. 12.** Phase portraits of the geostrophic stream-functions for the dominant low-frequency stable modes on the equatorial $\beta$-plane corresponding to Analytical Curve 2 (Fig. 7). The left panel represents the upper layer [$\psi_2 = \eta_1 + s\eta_2$], and the right panel represents the lower layer [$\psi_1 = \eta_1 + \eta_2$]. The velocity field is depicted with arrows. The modes shown include baroclinic Kelvin waves (top row) and baroclinic Yanai waves (bottom row), both for a wavenumber of $k = 4$.
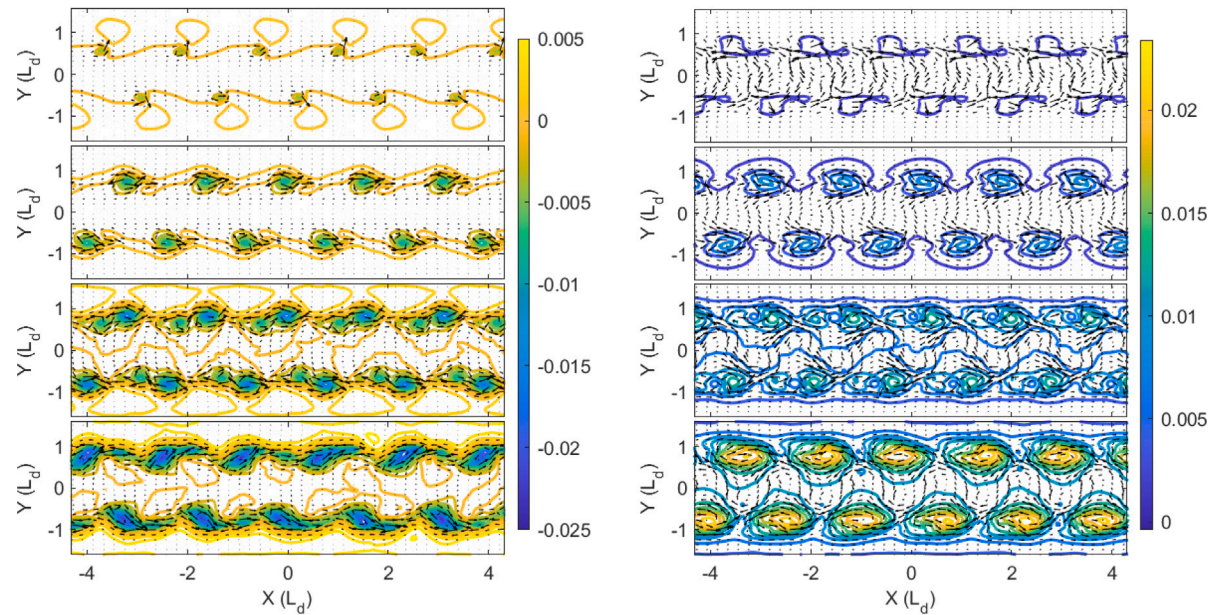


**Fig. 13.** Nonlinear evolution of pressure isopleths under diabatic conditions: The left and right panels display the perturbation in the lower and upper atmospheric layers, respectively, at times $T = 20, 40, 60, 80\,[1/\beta L_d]$ (from top to bottom). The simulations are initialized with a small fraction of the full periodic unstable mode, featuring a non-dimensional amplitude for $k = 4$.
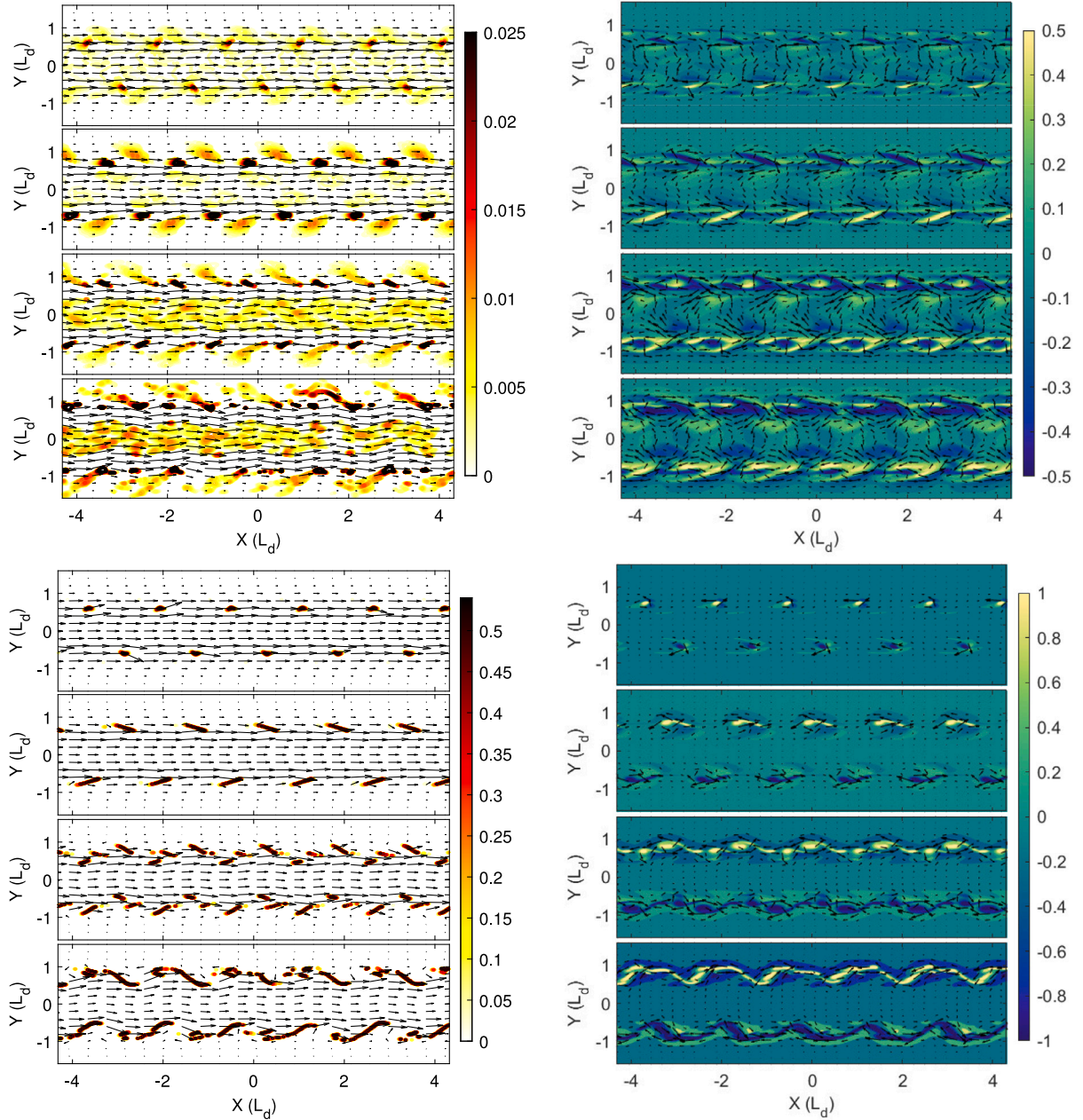
**Fig. 14.** *Upper row*: Tracer field of condensation (contours) and velocity field (arrows) in the upper layer (left panel), alongside the evolution of the relative vorticity (color) for the most unstable mode under diabatic conditions, with the corresponding velocity field indicated by arrows (right panel). Time $T = 20, 40, 60, 80 \, [1/\beta L_d]$ is shown from top to bottom. The simulations are initialized with a small fraction of the full periodic unstable mode, featuring a non-dimensional amplitude for $k = 4$. *Lower row*: The same diagnostics are presented for the lower layer. Note that the colorbars differ for better visibility.

an equatorial modon. Although the CCBKW maintains a higher phase velocity than the vortex pair, once the dipolar structure is established, it can sustain eastward propagation even in *dry* conditions, albeit with reduced speed due to dissipation and baroclinicity.

Fig. 19 illustrates the evolution of a persistent and coherent structure characterized by the coupling of a Kelvin wave with a dipole. The central region of this *hybrid structure*, positioned between the dipole and the CCBKW, constitutes the most convergent zone, which is identified as the primary condensation area, particularly during the initial stages (cf., see condensation patterns in Fig. 19). To the east and west of the hybrid center, regions of dense and depleted tracer fields are also discernible. The presence of low-level westerlies and easterlies in the western and eastern sectors of the *hybrid structure* further delineates the convective zone. Our analysis suggests that a

reduction in the intensity of moist convection induces a gap between the dipolar structure and the CCBKW, which is subsequently occupied by weak westerlies. In such instances, the detachment process is accompanied by a distinct double rainband structure. One of these rainbands propagates in tandem with the CCBKW, with its phase speed corresponding to that typical of CCBKWs. It is noteworthy that, in this iteration of the mcTRSW model, condensation is equivalent to precipitation and represents large-scale deep convection. At approximately $t \approx 35 \, [1/\beta L_d]$, the Kelvin wave begins to detach; however, it does not fully separate, with a significant portion of the wave remaining and interacting with the dipole. The dipole maintains its coherence and continues eastward propagation, though at a diminishing speed, and eventually ceases at $t \approx 85 \, [1/\beta L_d]$. Over time, the dipole's barotropic component intensifies and enlarges, reflecting
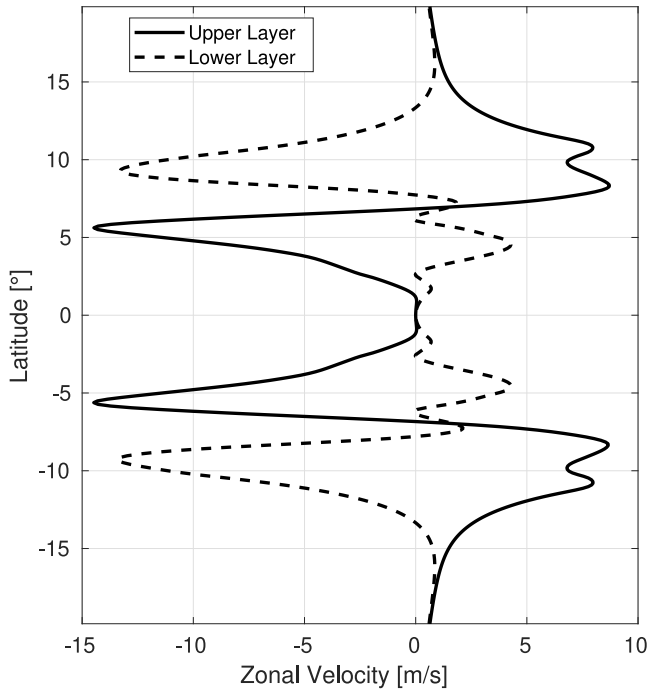
**Fig. 15.** Comparison of the nonlinear evolution of zonal velocity between the upper (solid line) and lower layer (dashed line) driven by the growth of the most unstable mode in a moist-convective environment. The plot shows the difference $[U_i(y) - U_{i0}(y)]$, averaged over 30 Jovian days, with both the x- and y-axes converted to dimensional units for clarity.

a trend towards barotropization. This transformation is influenced by interactions with inertia-gravity waves and Kelvin waves, as depicted in Fig. 20. The figure also shows a westward-propagating Rossby wave-like tail and an associated drying zone trailing behind the dipole. Despite its extended lifespan, this structure is categorized as a transient rather than a true modon due to its evolution through interactions with other wave modes and its barotropization. The figure highlights The phase speed of the baroclinic Kelvin wave is notably slower than that of the barotropic Kelvin wave. One of the key processes that significantly destabilizes the eastward propagation and contributes to the genesis of cyclones in the later stages is the collision of circumnavigated CCBKW with the eastward-propagating system. This interaction is clearly depicted in the Hovmöller diagram (Fig. 20). Such destabilization not only reduces the overall duration of eastward propagation but also triggers a series of smaller-scale, short-lived convective events. These events often result in the formation of westward-propagating cloud clusters. As these smaller convective envelopes increase in number during the later stages, some of them may merge, eventually forming tropical cyclones off the equator.

To investigate the effects of background zonal velocity, we examined the equatorial adjustment of large-scale localized negative and positive pressure anomalies in the presence of zonal jets, as depicted in Figs. 21 and 22. In both scenarios, a zonally elongated convective zone emerges at approximately 7.5° latitude in both hemispheres, where the most unstable modes grow due to slight deviations from the geostrophic balance state. In the case of the positive anomaly, the distribution of instability off the equator near 7.5° latitude is much more zonally broadened than in the negative anomaly scenario. This difference appears to stem from the stronger Rossby wave emergence during the adjustment of the positive anomaly. The configuration with the initial negative pressure anomaly persists with its negative equatorial center over a longer timescale compared to its positive counterpart. Fig. 23 demonstrates that following the departure of the

barotropic Kelvin wave (BTKW), the divergence patterns for simulations initialized with negative and positive pressure anomalies diverge significantly. The negative anomaly generates an equatorial convergence zone west of the convergent wings, whereas the positive anomaly produces a convergence zone east of the off-equatorial wings. It takes about two Jovian weeks for the barotropic Kelvin wave to circumnavigate Jupiter's periphery and interact with the emerging structures. Each passage generates secondary vortices off the equator for the negative disturbance configuration. Fig. 24, which depicts the pressure anomaly in the lower layer, illustrates a train of low-pressure systems near 7.5° latitude, accompanied by condensation zones. These low-pressure systems are represented by slowly eastward-propagating tilted lines in the Hovmöller diagram panels.

As previously mentioned, baroclinic and barotropic equatorial waves are anticipated as outcomes of the atmospheric adjustment processes simulated by the 2mcRSW model. Following Rostami and Zeitlin (2020), Appendix A reviews the linear long-wave spectrum of a two-layer reduced gravity shallow water (2RSW) system, both with and without moisture effects. The analysis begins by linearizing the *moist* system under the assumption of immediate relaxation of condensation. This assumption, relevant to tropical regions where relaxation times are short compared to the evolution times of large-scale systems, allows for a more straightforward examination of the wave spectrum. We utilize long-wave scaling to derive simplified equations for the zonal and meridional velocities, as well as for layer thickness perturbations. By applying linear transformations, the system is diagonalized, leading to expressions for the phase velocities of both barotropic and baroclinic modes. The analysis shows that the spectrum consists of fast barotropic Kelvin waves and slower baroclinic Kelvin and Rossby waves. The barotropic Kelvin waves propagate eastward with phase velocities at least three times greater than the westward-propagating baroclinic Kelvin and Rossby waves.

Some notable distinctions between the mechanism presented in this study and that of Legarreta et al. (2016) are outlined below:

(1) The mechanism proposed in this work is fundamentally modon-based, distinct from the Rossby–Kelvin-based structure described by Legarreta et al. (2016). This distinction underscores dynamical differences between the two approaches.

(2) In the one-layer RSW model proposed by Legarreta et al. (2016), equatorial disturbances lead to the formation of symmetric Rossby lobes that propagate westward relative to the disturbance source. These lobes detach over time, while Kelvin waves propagate eastward. Our mechanism exhibits similar behavior under dry adiabatic conditions. However, in the moist-convective regime, once a critical threshold of negative pressure anomaly is surpassed, a coherent dipolar structure–distinct from the Y-shaped structure–emerges and propagates eastward. This dipolar entity, termed the equatorial modon, is robust, self-sustaining, and maintains its form during propagation, even under dry adiabatic conditions (Rostami and Zeitlin, 2019b).

(3) Moist convection is essential for initiating the eastward propagation in the modon-based mechanism, while in the framework proposed by Legarreta et al. (2016), moist-convective processes do not appear to be a critical factor for the wave dynamics.

(4) The equatorial modon has an exact linear solution in terms of leading-order velocity, referred to as the asymptotic modon (see Fig. 25). Once initialized, this structure inherently propagates eastward, distinguishing itself from Rossby waves, which exhibit westward propagation. A detailed analytic solution of the asymptotic modon's structure can be found in Appendix C.

(5) In the two-layer RSW model of Legarreta et al. (2016), a background zonal wind is consistently included in their simulations. In contrast, our experiments demonstrate that eastward propagating systems can be generated both with and without an imposed background velocity field.
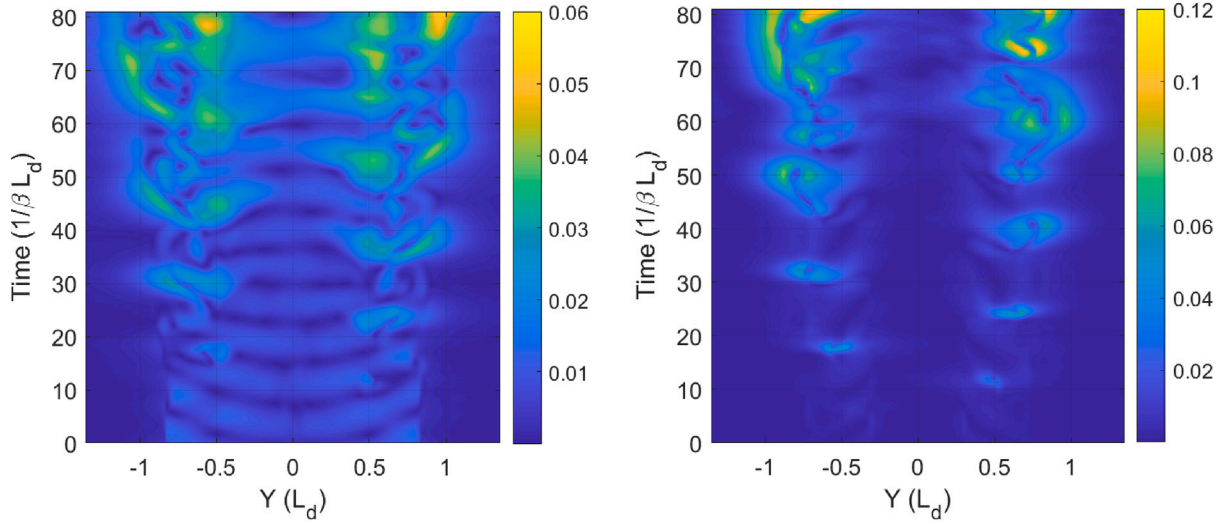
**Fig. 16.** *Left panel*: Hovmöller diagram of the kinetic energy of the growing perturbation along $X = 0$ for the upper (left panel) and lower (right panel) layers under moist convection in the lower layer. The simulations are initialized with a small fraction of the full periodic unstable modes, with a small non-dimensional amplitude for $k = 4$. The vertical axis represents latitude, with $Y = 0$ indicating the equator.
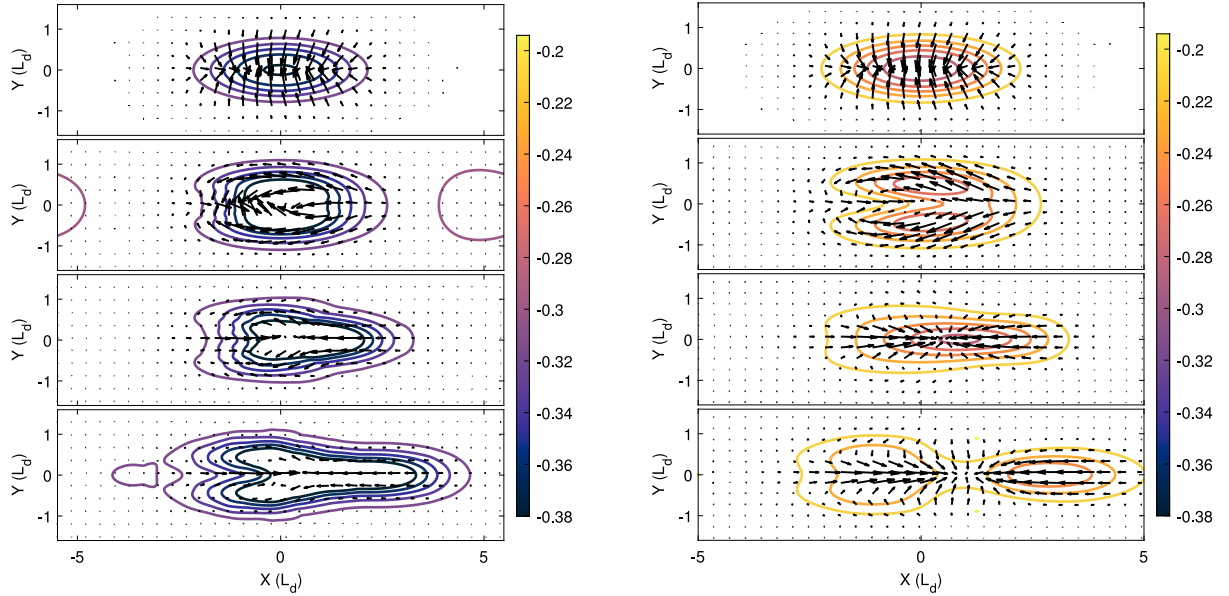


**Fig. 17.** *Left panel*: Initial stages of equatorial adjustment of a negative pressure anomaly in the lower layer, depicted through the evolution of baroclinic velocity (arrows) and $\eta_{bc}$ (contours) in a moist-convective environment at times $t = 0.5, 5, 10, 20\,[1/\beta L_d]$. *Right panel*: The same diagnostic for the *dry* case.

## 6. Summary, discussion, and conclusions

This study analyzes the interaction between ammonia-driven moist convection in the shallow upper atmosphere and large-scale dynamics in Jupiter's Equatorial Zone using an idealized two-layer moist convective Rotating Shallow Water (2mcRSW) model.

We investigated the stability properties of a two-layer jet configuration in a geostrophically balanced state, examining both barotropic and baroclinic scenarios. The barotropic stability analysis revealed that the mean zonal velocity profiles and thickness deviations could be represented by analytical curves, with the most unstable modes typically corresponding to zonal wavenumbers 4 to 7. As zonal winds intensified, the most unstable modes shifted to lower wavenumbers. The pressure fields of the most unstable modes display symmetric patterns resembling Rossby waves at the poleward edges of the zonal jets. This behavior remained consistent with stronger jet velocities.

The most unstable modes in the baroclinic configuration also corresponded to zonal wavenumbers 4 to 6, with a trend towards lower wavenumbers as zonal velocities increased. The presence of shear between the two layers enhanced the instability growth rates. The unstable modes displayed cyclonic and anticyclonic rotation patterns in their geostrophic streamfunctions, with intensified cyclonic components in the lower layer and corresponding anticyclonic components in the upper layer. A comparison between the barotropic and baroclinic analyses indicated that baroclinic instability exhibited lower phase velocities compared to the barotropic case. Stability diagrams for baroclinic structures demonstrated that instability trends shifted to lower wavenumbers with increased disturbances, mirroring the barotropic findings. Dispersion relations revealed various equatorial waves, including barotropic and baroclinic Kelvin waves, Rossby waves, Mixed Rossby-Gravity waves, and Inertia-Gravity waves, each with distinct propagation characteristics across different dynamic regimes.
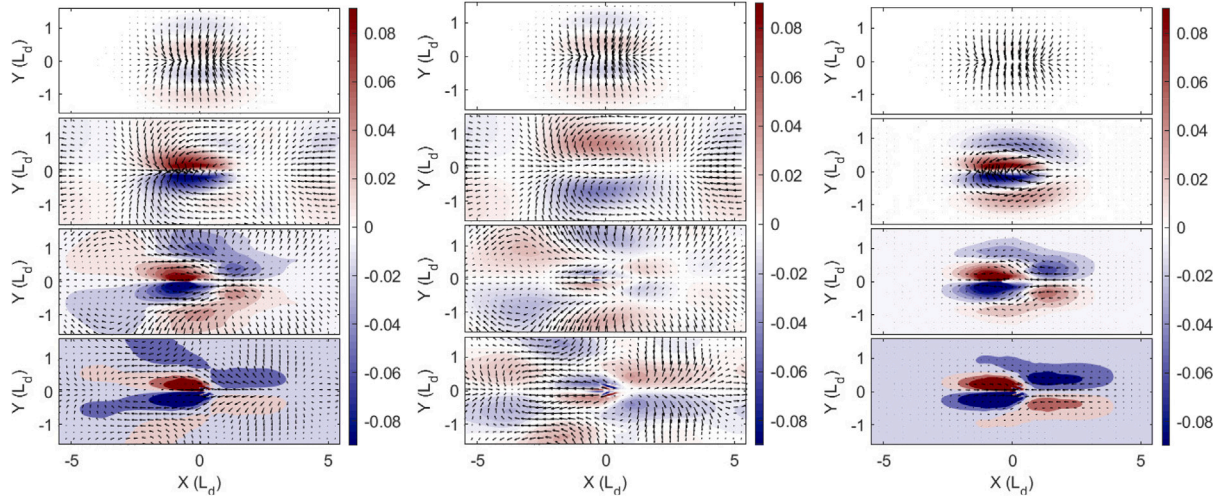
**Fig. 18.** Nonlinear evolution of equatorial adjustment at the initial stages, triggered by a negative pressure anomaly in the lower layer, depicted through relative vorticity in the lower (left panel), upper (middle panel), and baroclinic (right panel) layers in a moist-convective environment at times $t = 0.5, 5, 10, 20 \, [1/\beta L_d]$ (from top to bottom).
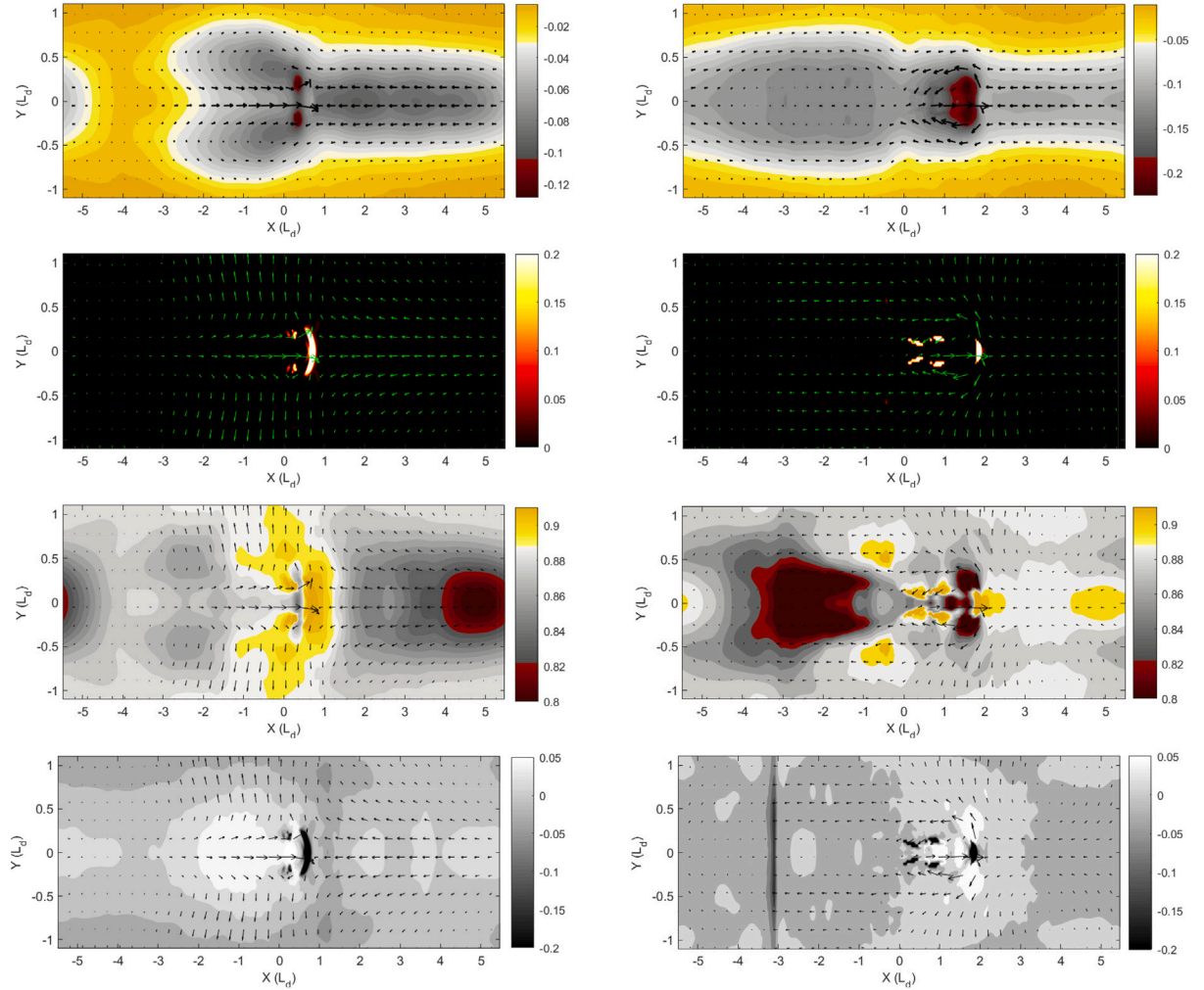


**Fig. 19.** *First row*: Late stages of the eastward-propagating *hybrid structure*, as depicted by the baroclinic pressure anomaly (colors) and baroclinic velocity (arrows), at times $t = 35, 85 \, [1/\beta L_d]$ in moist-convective environments, shown from left to right. *Second row*: Corresponding condensation patterns. *Third row*: Distribution of humidity (colors) in the lower layer, along with the corresponding velocity field (arrows). *Lower row*: Divergence in the lower layer. The initial conditions and parameter values are consistent with those in Fig. 17. (For interpretation of the references to color in this figure legend, the reader is referred to the web version of this article.)
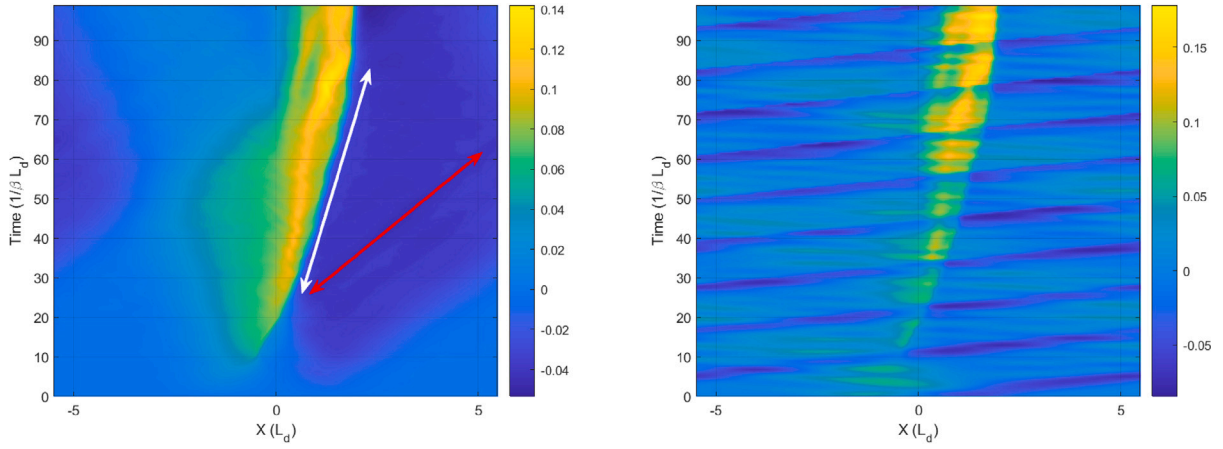
**Fig. 20.** Hovmöller diagrams illustrating the zonal velocity components: baroclinic (left panel) and barotropic (right panel). White arrows denote the eastward propagation of the dipole, while red arrows indicate the movement of the baroclinic Kelvin wave. The initial conditions are identical to those in Fig. 17. (For interpretation of the references to color in this figure legend, the reader is referred to the web version of this article.)
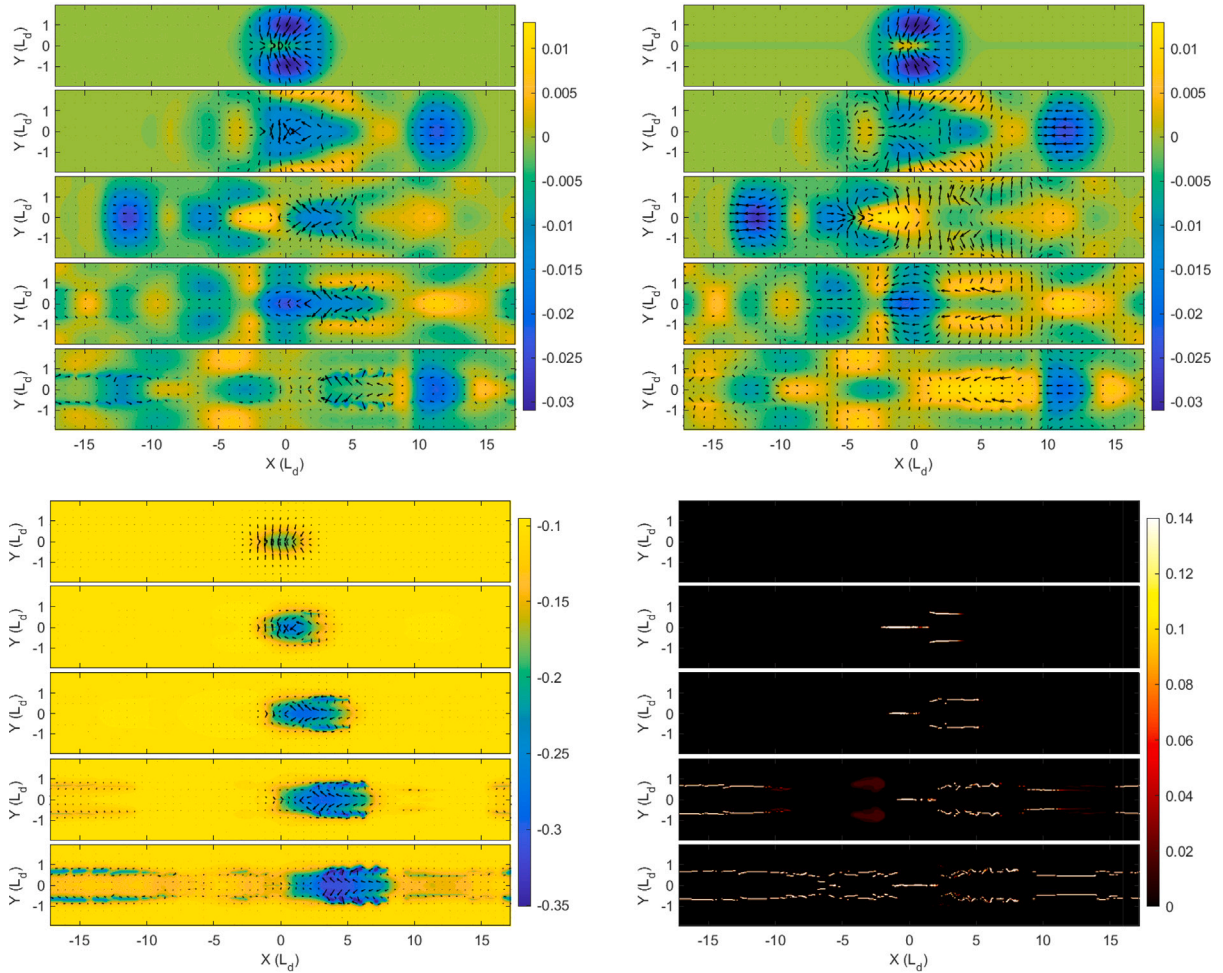


**Fig. 21.** *First row*: Evolution of the depression in the lower (left panel) and upper (right panel) layers, with corresponding velocity fields indicated by arrows. *Second row*: Baroclinic anomaly of the disturbance (left panel) with its velocity field (arrows) and associated condensation patterns (right panel). Times $t = 1, 10, 20, 30, 40\,[1/\beta L_d]$ are shown sequentially from top to bottom in all panels. All initial conditions are in the presence of a mean flow in a moist-convective environment.

The nonlinear simulations, initiated with a background zonal velocity profile and a small perturbation at wavenumber $k = 4$, offer critical insights into the dynamics of moist-convective flows in Jupiter's atmosphere. The growth of the unstable mode leads to the intensification of vortical structures, with cyclonic vortices forming in the lower layer and anticyclonic vortices in the upper layer. Moist convection drives condensation, increasing kinetic energy in the lower layer and supporting the hypothesis of net rising motion in the belts. Condensation patterns highlight both large-scale regions and localized moist convective patches driven by shear velocity, manifesting as lightning
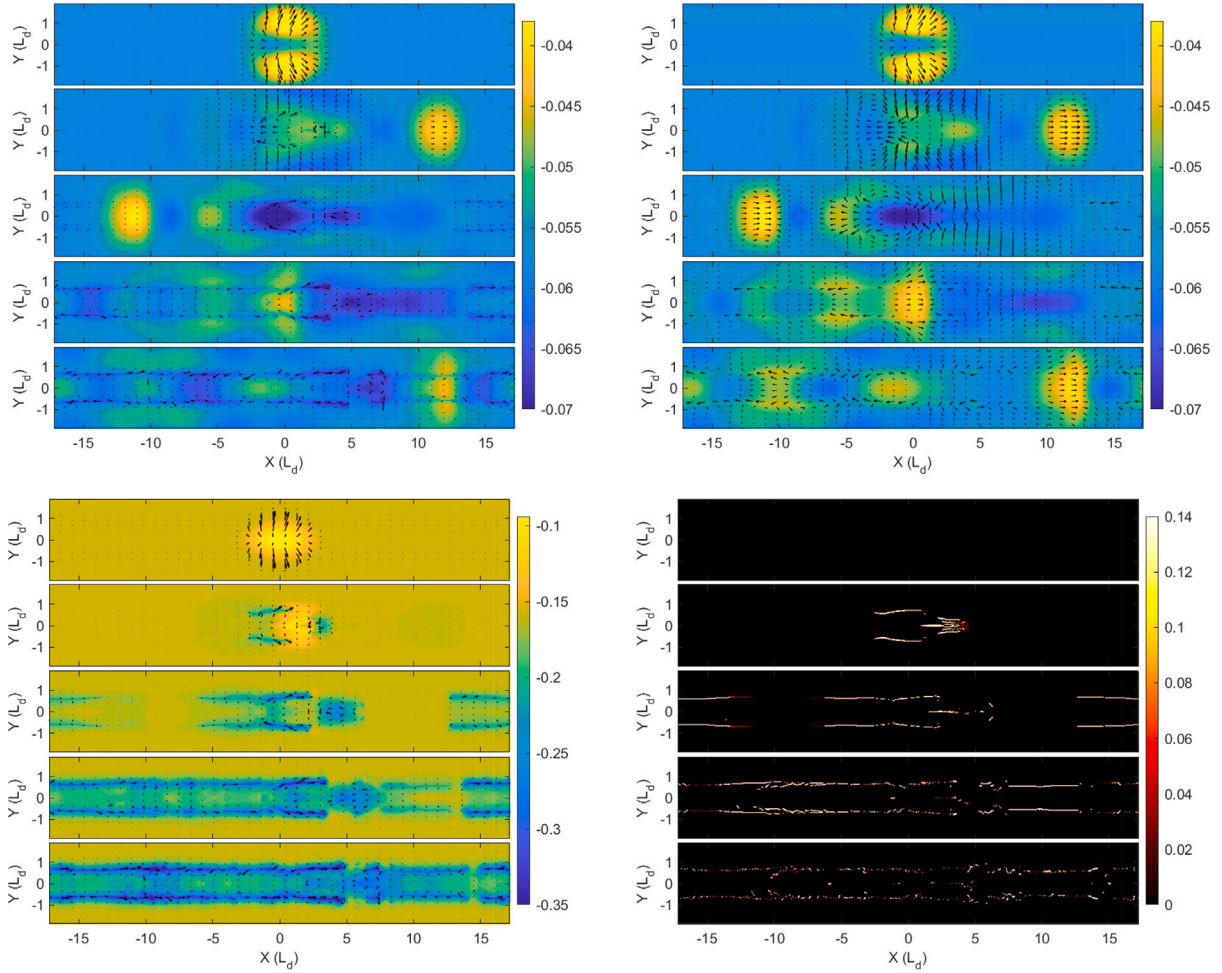
**Fig. 22.** Diagnostics analogous to those in Fig. 21, but for a positive anomaly disturbance.
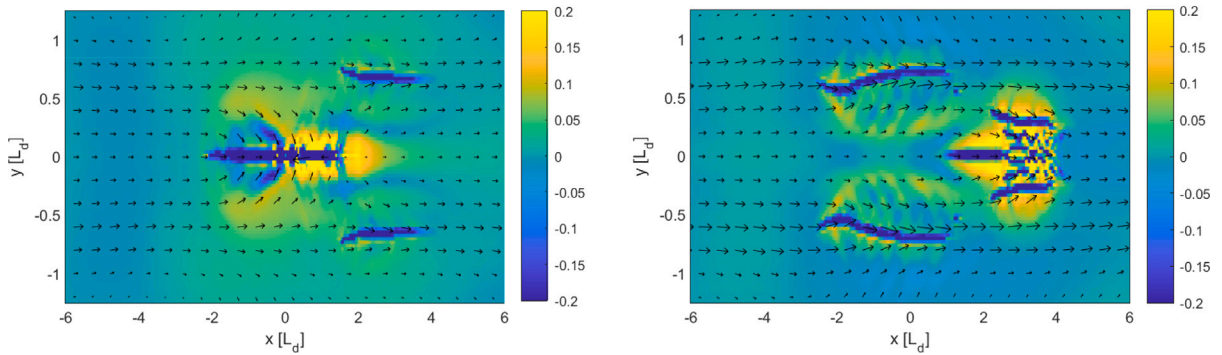


**Fig. 23.** Comparison of the divergence field for simulations with initial negative (left panel) and positive (right panel) pressure anomaly disturbances in the lower layer, along with the corresponding velocity fields depicted as arrows, at time $10\,[1/\beta L_d]$. Both initial conditions are set in the presence of mean flow within a moist-convective environment.

and high white cloud clusters, though Jovian lightning predominantly occurs at higher latitudes.

The simulations further demonstrate a significant intensification of vertical shear zonal velocity during active convection, more pronounced in the moist-convective environment compared to the *dry* case. Additionally, a smooth poleward drift of emerged instabilities under diabatic conditions is observed, diverging from observational data as discussed in Section 4. The dynamics suggest a strong linkage between the kinetic energy of upper-layer anticyclones and lower-layer cyclones, with the latter driving the poleward motion of the former. The alignment between simulated lightning, convection, and

instability strongly indicates that Jovian lightning likely occurs in the most unstable regions.

We have provided a novel explanation for the formation of the Y-shaped cloud structures observed near Jupiter's equator. Legarreta et al. (2016)'s interpretation of these eastward-propagating features was based on the Matsuno–Gill mechanism, which requires a background zonal wind. However, we propose that these structures result from the interaction between a baroclinic equatorial modon and convectively driven Kelvin waves within a moist-convective environment. A modon, in this context, refers to a coherent bipolar structure with eastward propagation. Our simulations reveal that when localized
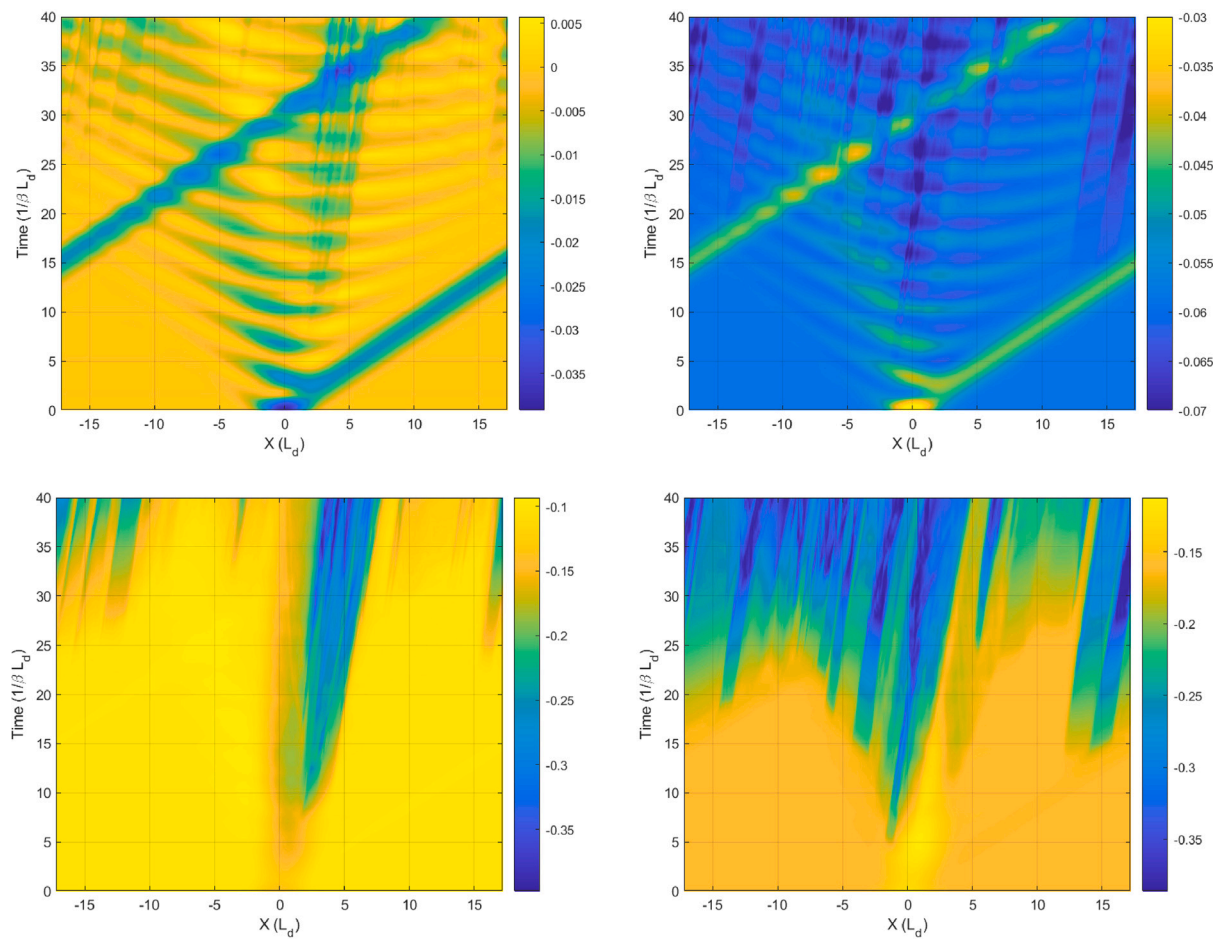
**Fig. 24.** *First row*: Comparison of the Hovmöller diagram of pressure anomalies in the lower layer at the equator for negative (left panel) and positive (right panel) disturbances. *Second row*: Baroclinic pressure anomalies for the negative (left panel) and positive (right panel) disturbances. Both initial conditions are set in the presence of mean flow within a moist-convective environment.
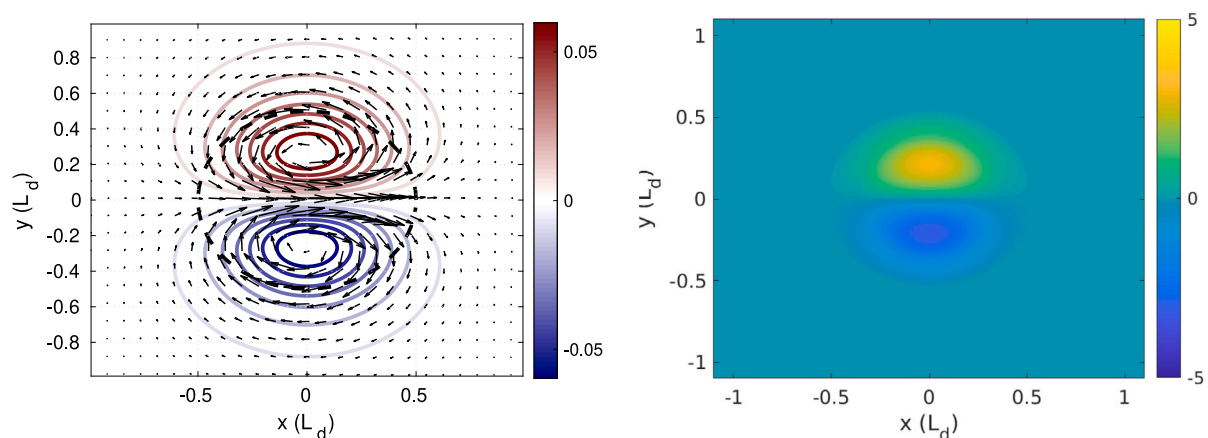


**Fig. 25.** Streamlines and velocity field of an asymptotic modon (left panel) alongside its relative vorticity (right panel) with $U = 0.1$. The dashed circle indicates the separatrix with a radius of $a = 0.5$.

large-scale heating occurs in Jupiter's moist-convective environment, it triggers an equatorial adjustment process that produces a baroclinic equatorial modon. This modon, coupled with a detaching convectively coupled baroclinic Kelvin wave (CCBCKW), forms a *hybrid structure* that bears a resemblance to the Y-shaped cloud formations observed. In moist-convective environments, the coupling between the modon and the CCBCKW is more persistent, leading to a longer-lasting Y-shaped structure. In contrast, in drier environments, the CCBCKW

detaches earlier, resulting in a shorter-lived formation. Additionally, the study demonstrates that the background zonal velocity influences the development and morphology of these structures. The presence of zonal jets alters the location and intensity of equatorial convergence zones, thereby affecting the interaction between pressure anomalies and CCBCKW. This interaction can give rise to secondary vortices and short-lived convective events, occasionally leading to the formation of

tropical cyclones. In this mechanism, a background zonal wind is not a necessary condition for the formation of the Y-shaped structure.

Concerning the recurrent generation of Y-shaped structures, which has not been explicitly demonstrated in this study, we anticipate a mechanism similar to that proposed by Rostami et al. (2022). Specifically, when a CCBKW, after circumnavigating the Equator, interacts with a new large-scale positive buoyancy anomaly or negative pressure anomaly, this interaction can trigger the recurrent generation of a new eastward-propagating *hybrid structure*. The intensity and extent of the diabatic processes associated with the coupled structures in each episode – and consequently, the degree of CCBKW deceleration – vary. Therefore, it is unsurprising that the Y-shaped structure in this mechanism is not a regular periodic oscillation but rather an episodic weather event.

## CRediT authorship contribution statement

**Masoud Rostami:** Writing – original draft, Visualization, Validation, Supervision, Software, Project administration, Methodology, Investigation, Formal analysis, Data curation, Conceptualization. **Bijan Fallah:** Writing – original draft, Visualization, Validation, Software, Methodology, Formal analysis, Data curation. **Farahnaz Fazel-Rastgar:** Writing – review & editing, Validation, Software, Methodology, Investigation, Conceptualization.

## Open research

The two-layer moist-convective Rotating Shallow Water (2mcRSW) model utilized in this study is openly accessible via ZENODO at https://doi.org/10.5281/zenodo.10054154.

## Declaration of competing interest

The authors declare no competing interests. This research was conducted without any commercial or financial relationships that could be perceived as a potential conflict of interest.

## Acknowledgments

## Appendix A. Linear long-wave spectrum

As discussed extensively in the literature, e.g., (Zeitlin, 2018), in the *dry* two-layer reduced gravity shallow water (2RSW) system, the spectrum of linear waves exhibits a duplication of each wave mode, characterized by corresponding barotropic and baroclinic modes. In the *moist* system described by Eq. (2.1), the condensation $C$ is a nonlinear function of the specific humidity $Q$. However, in the limit of immediate relaxation – relevant to the tropics where the relaxation time is typically on the order of a few hours for deep convection, which is short compared to the characteristic evolution times of large-scale systems – Eq. (2.1e) simplifies in the absence of evaporation to:

$$\tau \to 0 \;\Rightarrow\; C \to -Q_s \boldsymbol{\nabla} \cdot \boldsymbol{v}, \tag{A.1}$$

which permits a straightforward linearization of the system. The concept of immediate relaxation, and the simplification (A.1) it enables, is rooted in the work of Gill (1982). The mathematical properties of the resulting linearized system were thoroughly analyzed by Lambaerts et al. (2011b). To derive the wave spectrum, we adopt the long-wave scaling introduced by Le Sommer et al. (2004) and adapt it to our two-layer system. Note that this scaling is different from that used in the numerical simulations discussed earlier. We introduce a meridional

scale $L$ and a small aspect ratio $\delta$ (meridional to zonal), and also a slow time-scale $T$:

$$y \sim L, \quad x \sim \delta^{-1}L, \quad t \sim T = (\delta\beta L)^{-1}, \quad \delta \ll 1. \tag{A.2}$$

The velocity is scaled as:

$$u_i \sim U, \quad v_i \sim \delta U, \tag{A.3}$$

and we introduce nonlinearity parameters governing deviations $\eta_i$ from their equilibrium values:

$$h_i = H_i(1 + \lambda_i \eta_i). \text{ (no summation over i)} \tag{A.4}$$

We assume a parameter regime where nonlinearity and Rossby number are of the same order:

$$\lambda_1 \sim \lambda_2 \sim \epsilon = \frac{U}{\beta L^2}, \quad \frac{gH}{(\beta L^2)^2} \sim 1. \tag{A.5}$$

Here, $\epsilon$ represents the equatorial Rossby number. With this scaling, and under the hypothesis of immediate relaxation (A.1), the Eqs. (2.1) are simplified to:

$$\begin{cases} \partial_t u_i + \epsilon(\boldsymbol{v}_i \cdot \boldsymbol{\nabla})u_i - yv_i = -\partial_x(\eta_1 + s^{i-1}d\,\eta_2) + \mathcal{O}(\epsilon^2) \\ \delta^2[\partial_t v_i + \epsilon(\boldsymbol{v}_i \cdot \boldsymbol{\nabla})v_i] + yu_i = -\partial_y(\eta_1 + s^{i-1}d\,\eta_2) + \mathcal{O}(\delta\epsilon, \epsilon^2) \\ \partial_t \eta_i + \left[1 + (-1)^i \frac{\gamma Q^s}{H_i}\right]\boldsymbol{\nabla}\cdot\boldsymbol{v}_i + \epsilon\boldsymbol{\nabla}\cdot(\eta_i\boldsymbol{v}_i) = 0 + \mathcal{O}(\delta\epsilon, \epsilon^2), \end{cases} \tag{A.6}$$

where $i = 1, 2$. The parameters $\gamma Q^s/H_i$ characterize convective activity. We introduce $\kappa = \gamma Q^s/H_1$ for convenience. Here, $d = H_2/H_1$ denotes the ratio of non-perturbed layer thicknesses. We separate the equations for zonal and meridional velocity components and thickness perturbations, omitting higher-order terms. Assuming $\epsilon \sim \delta^2$, we obtain the linearized system:

$$\begin{cases} \partial_t u_i - yv_i = -\partial_x(\eta_1 + s^{i-1}d\,\eta_2) \\ +yu_i = -\partial_y(\eta_1 + s^{i-1}d\,\eta_2) \\ \partial_t \eta_i + \left[1 + (-1)^i \frac{\gamma Q^s}{H_i}\right]\boldsymbol{\nabla}\cdot\boldsymbol{v}_i = 0. \end{cases} \tag{A.7}$$

A linear transformation of the form:

$$\boldsymbol{v}_\pm = \boldsymbol{v}_1 + A_\pm\boldsymbol{v}_2, \quad \eta_\pm = \eta_1 + B_\pm\eta_2 \tag{A.8}$$

can diagonalize the system (A.7):

$$\begin{cases} \partial_t u_\pm - yv_\pm + a_\pm\partial_x\eta_\pm = 0, \\ \partial_t v_\pm + yu_\pm + a_\pm\partial_y\eta_\pm = 0, \\ \partial_t \eta_\pm + b_\pm\boldsymbol{\nabla}\cdot\boldsymbol{v}_\pm = 0, \end{cases} \tag{A.9}$$

where:

$$a_\pm = 1 + A_\pm, \quad b_\pm = 1 - \kappa \tag{A.10}$$

By comparing Eqs. (A.7) and (A.9), we find:

$$B_\pm = \frac{d(1 + sA_\pm)}{1 + A_\pm}, \quad A_\pm = \frac{B_\pm(1 + \frac{\kappa}{d})}{1 - \kappa} \tag{A.11}$$

In the absence of moist convection, $B_\pm \equiv A_\pm$, and $1 - \kappa$ represents the non-dimensional moist enthalpy, which must remain positive. Solving these algebraic equations yields:

$$A_\pm = \frac{(\sigma s - 1)}{2} \pm \sqrt{\frac{(\sigma s - 1)^2}{4} + \sigma} \tag{A.12}$$

where $\sigma = (d + \kappa)/(1 - \kappa)$. Without moist convection, $\sigma \equiv d$, indicating that moist convection effectively increases the ratio $d$ by reducing $H_1$. The value of $B_\pm$ is determined from the first Eq. in (A.11). For $s - 1 = \Delta \ll 1$, which is the scenario considered here, $A_+ = d + \mathcal{O}(\Delta)$ and $A_- = -1 + \mathcal{O}(\Delta)$ in the *dry* configuration. The baroclinic component is approximately the difference between the upper and lower layers. The phase velocity squared is given by:

$$c_\pm^2 = \left(\frac{(\sigma s + 1)}{2} \pm \sqrt{\frac{(\sigma s - 1)^2}{4} + \sigma}\right)(1 - \kappa) \tag{A.13}$$

It is important to note that for statically stable configurations with $s > 1$, the product $a_{\pm}b_{\pm}$ is positive, and the system is hyperbolic if the linearized moist enthalpy $M = H_1 - \gamma Q^s$ is positive. The subscript $-(+)$ corresponds to the baroclinic (barotropic) mode. As shown by Lambaerts et al. (2011b), moist baroclinic modes are always slower than their *dry* counterparts. In cases of weak stratification, where $s$ is close to one, $A_{\pm}$ and $B_{\pm}$ are close to $-1$, and thickness ratios are on the order of 1.

Following the demonstration in Le Sommer et al. (2004) (also see Zeitlin (2018), ch. 5), it can be shown that the general solution of the system (A.9) for both barotropic and baroclinic modes includes a mean zonal flow, which we will not address further, and equatorial Kelvin waves with a meridional structure $\phi_0(y/\sqrt{c_{\pm}})$, propagating eastward with phase velocity:

$$c_{\pm} = \sqrt{a_{\pm}b_{\pm}} \tag{A.14}$$

and equatorial Rossby waves with meridional structure $\phi_n(y/\sqrt{c_{\pm}})$, propagating westward with phase velocities:

$$c_n = \frac{c_{\pm}}{2n+1}, \quad n = 1, 2, \ldots \tag{A.15}$$

Here, $\phi_n$ are Gauss–Hermite (parabolic cylinder) functions that describe the meridional structure of waves on the equatorial beta-plane.

In summary, the spectrum of long linear waves in the model comprises fast barotropic Kelvin waves and slow baroclinic Kelvin and Rossby waves. The former propagate eastward with phase velocities at least three times greater than the latter, which propagate westward.

## Appendix B. Initialization of the equatorial disturbance

The initial pressure distributions in the layers, denoted as $h_i = H_i(x, y)$, were derived using the alpha-Gaussian profile centered at the equator, following Rostami and Zeitlin (2017). This profile is particularly advantageous as it allows precise control over both the spatial extent and the steepness of the distribution. While the sensitivity of the adjustment process to these parameters has been documented (Rostami and Zeitlin, 2019b), a detailed exploration of this sensitivity lies beyond the scope of the present work.

The normalized, axisymmetric alpha-Gaussian thickness distribution is expressed as:

$$H_i(r, \sigma) = 1 + \lambda_i \frac{2^{1/\sigma}}{\sigma} \Gamma\left(\frac{1}{\sigma} + \frac{1}{2}\right) G\left(\frac{r^{\sigma}}{2}, \frac{1}{\sigma} + \frac{1}{2}\right), \tag{B.1}$$

where $r = \sqrt{x^2 + y^2}$, $G(r, b) = \left[1/\Gamma(b)\right] \int_r^b e^{-t} t^{b-1} \, dt$, and $\Gamma$ is the gamma function. The parameters $\lambda_i$ and $\sigma$ define the amplitude and steepness of the pressure anomaly, with the maximum anomaly $\Delta H/H_0$, where $H_0$ is the unperturbed total depth, being dependent on both. Although $\lambda_i$ can be positive or negative, this study focuses on negative pressure perturbations within the lower layer only. By stretching the zonal coordinate $x \to a^{-1} x$ in $H_i(x, y)$, a perturbation with a zonal-to-meridional aspect ratio $a$ is obtained. The amplitude, steepness, and aspect ratio of the initial perturbation are adjustable parameters, with steepness fixed at $\sigma = 3$ in this study.

The zonal extent of the anomaly in the simulations presented here is approximately $4 L_d$, where $L_d$ is the horizontal length scale, defined by $L_d^2 = \sqrt{gH_0}/\beta$, with $H_0 = H_1 + H_2$. The non-dimensional layer thicknesses were chosen as $H_1 = 0.35$ and $H_2 = 0.65$. Numerical simulations were conducted using the finite-volume method of Bouchut and Zeitlin (2010) on a $500 \times 500$ regular grid over a domain of $11L_d \times 12L_d$ on the equatorial beta-plane. The zonal extent of the domain corresponds to the circumference of the equator, with periodic boundary conditions applied in this direction. The exaggerated meridional extent allows for the efficient implementation of sponge boundary conditions, which absorb short and fast inertia-gravity waves generated during the adjustment process.

## Appendix C. Summary of the analytic solution of the asymptotic modon's structure

We recall that the equation governing the stream function of the equatorial modon is derived from the RSW equations in the equatorial beta-plane under the assumption of negligible dissipation:

$$\begin{cases} \partial_t \mathbf{v} + \mathbf{v} \cdot \nabla \mathbf{v} + \beta y \hat{\mathbf{k}} \wedge \mathbf{v} + g \nabla h = 0, \\ \partial_t h + \nabla \cdot (\mathbf{v} h) = 0, \end{cases} \tag{C.1}$$

where $\nabla = (\partial_x, \partial_y)$, $\mathbf{v} = (u, v)$, with $u$ and $v$ representing the zonal and meridional components of velocity, respectively. Here, $h$ denotes the geopotential height, $\beta$ signifies the meridional gradient of the Coriolis parameter, and $\hat{\mathbf{k}}$ is the unit vector in the vertical direction. A small pressure perturbation ($\lambda \to 0$) can be incorporated into the equations through the parameter $\lambda$: $h = H(1 + \lambda \eta)$, where $H$ represents the unperturbed geopotential height. The characteristic spatial, velocity, and temporal scales are given by $(x, y) \sim L$, $(u, v) \sim V$, $t \sim L/V$. Assuming that the characteristic velocity is significantly smaller than the phase velocity of the barotropic Kelvin waves, $c = \sqrt{gH}$, such that $V \ll \sqrt{gH}$ and $(gH\lambda)/V^2 = \mathcal{O}(1)$, we find that the non-dimensional equations take the following form:

$$\partial_t \mathbf{v} + \mathbf{v} \cdot \nabla \mathbf{v} + \overline{\beta} y \hat{\mathbf{k}} \wedge \mathbf{v} + \nabla \eta = 0. \tag{C.2}$$

$$\lambda \left( \partial_t \eta + \mathbf{v} \cdot \nabla \eta \right) + (1 + \lambda \eta) \nabla \cdot \mathbf{v} = 0. \tag{C.3}$$

Here, $\overline{\beta} = (\beta L^2)/V$, and $\mathbf{v} = \mathbf{v}_0 + \lambda \mathbf{v}_1 + \cdots$. In the leading order in $\lambda$, the Eq. (C.3) leads to $\nabla \cdot \mathbf{v}_0 = 0$, indicating that the flow is non-divergent. Consequently, we express the velocities as $u_0 = -\partial_y \psi$, and $v_0 = \partial_x \psi$. The stream function can be derived through cross-differentiation of the zonal and meridional momentum equations:

$$\nabla^2 \psi_t + \mathcal{J}(\psi, \nabla^2 \psi) + \overline{\beta} \psi_x = 0, \tag{C.4}$$

where $\mathcal{J}$ denotes the Jacobian operator. The modon solutions are obtained under the assumption of steady motion characterized by a constant zonal velocity $U$. This is achieved by positing a linear relationship between the absolute vorticity and the stream function in the co-moving frame, yielding an inhomogeneous Helmholtz equation. This equation is solved via separation of variables in polar coordinates, utilizing Bessel functions. The solution is first derived in the outer domain under the decay condition and subsequently in the inner domain, with matching conditions applied across a circle of a specified radius $a$ in the plane. The solution is expressed as:

$$\begin{cases} \psi_{\text{ext}} = -\frac{Ua}{K_1(pa)} K_1(pr) \sin\theta, \quad r > a, \\ \psi_{\text{int}} = \left[ \frac{Up^2}{v^2 J_1(va)} J_1(vr) - \frac{r}{v^2}(1 + U + Uv^2) \right] \sin\theta, \quad r < a. \end{cases} \tag{C.5}$$

In this expression, $J_1$ and $K_1$ denote the ordinary and modified Bessel functions of order one, respectively. The parameter $p$ is real, with $p^2 = \overline{\beta}/U$. The condition $U > 0$ indicates that the motion is directed *eastward*. For each pair $(a, p)$, a series of eigenvalues $v$ arises from the matching conditions, with the lowest eigenvalue corresponding to a dipolar structure, termed the asymptotic modon. The subsequent eigenvalue yields a quadrupolar solution known as the *shielded modon*, and further eigenvalues correspond to multipolar vortices characterized by pronounced velocity shears within the core, which exhibit increased sensitivity to dissipation. Centering the solution within the equatorial beta-plane results in a cyclonic pair. The streamlines of the asymptotic modon, as determined by Eqs. (C.5), are illustrated in Fig. 25.

## Data availability

Data will be made available on request.

# References

Achterberg, R.K., Conrath, B.J., Gierasch, P.J., 2006. Cassini CIRS retrievals of ammonia in Jupiter's upper troposphere. Icarus 182 (1), 169–180, URL https://www.sciencedirect.com/science/article/pii/S0019103505005087.

Antuñano, A., Fletcher, L.N., Orton, G.S., Melin, H., Rogers, J.H., Harrington, J., Donnelly, P.T., Rowe-Gurney, N., Blake, J.S.D., 2018. Infrared characterization of jupiter's equatorial disturbance cycle. Geophys. Res. Lett. 45 (20), 10,987–10,995, URL https://agupubs.onlinelibrary.wiley.com/doi/abs/10.1029/2018GL080382.

Atreya, S., Wong, M., Owen, T., Mahaffy, P., Niemann, H., de Pater, I., Drossart, P., Encrenaz, T., 1999. A comparison of the atmospheres of Jupiter and Saturn: deep atmospheric composition, cloud structure, vertical mixing, and origin. Planet. Space Sci. 47 (10), 1243–1262, URL https://www.sciencedirect.com/science/article/pii/S0032063399000471.

Banfield, D., Gierasch, P., Bell, M., Ustinov, E., Ingersoll, A., Vasavada, A., West, R.A., Belton, M., 1998. Jupiter's cloud structure from Galileo imaging fata. Icarus 135 (1), 230–250, URL http://www.sciencedirect.com/science/article/pii/S0019103598959851.

Barrado-Izagirre, N., Rojas, J.F., Hueso, R., Sánchez-Lavega, A., Colas, F., Dauvergne, J.L., Peach, D., IOPW-Team, 2013. Jupiter's zonal winds and their variability studied with small-size telescopes. Astron. Astrophys. 554 (1), 11. http://dx.doi.org/10.1051/0004-6361/201321201.

Becker, H.N., Alexander, J.W., Atreya, S.K., Bolton, S.J., Brennan, M.J., Brown, S.T., Guillaume, A., Guillot, T., Ingersoll, A.P., Levin, S.M., Lunine, J.I., Aglyamov, Y.S., Steffes, P.G., 2020. Small lightning flashes from shallow electrical storms on Jupiter. Nature 584 (7819), 55–58. http://dx.doi.org/10.1038/s41586-020-2532-1.

Betts, A.K., Miller, M.J., 1986. A new convective adjustment scheme. Part II: Single column tests using GATE wave, BOMEX, ATEX and arctic air-mass data sets. Q. J. R. Meteorol. Soc. 112 (473), 693–709, URL https://rmets.onlinelibrary.wiley.com/doi/abs/10.1002/qj.49711247308.

Boissinot, A., Spiga, A., Guerlet, S., Cabanes, S., Bardet, D., 2024. Global climate modeling of the Jupiter troposphere and effect of dry and moist convection on jets. Astron. Astrophys. 687, A274. http://dx.doi.org/10.1051/0004-6361/202245220.

Bolton, S.J., Adriani, A., Adumitroaie, V., Allison, M., Anderson, J., Atreya, S., Bloxham, J., Brown, S., Connerney, J.E.P., DeJong, E., Folkner, W., Gautier, D., Grassi, D., Gulkis, S., Guillot, T., Hansen, C., Hubbard, W.B., Iess, L., Ingersoll, A., Janssen, M., Jorgensen, J., Kaspi, Y., Levin, S.M., Li, C., Lunine, J., Miguel, Y., Mura, A., Orton, G., Owen, T., Ravine, M., Smith, E., Steffes, P., Stone, E., Stevenson, D., Thorne, R., Waite, J., Durante, D., Ebert, R.W., Greathouse, T.K., Hue, V., Parisi, M., Szalay, J.R., Wilson, R., 2017. Jupiter's interior and deep atmosphere: The initial pole-to-pole passes with the Juno spacecraft. Science 356 (6340), 821–825.

Borucki, W.J., Williams, M.A., 1986. Lightning in the Jovian water cloud. J. Geophys. Res.: Atmos. 91 (D9), 9893–9903, URL https://agupubs.onlinelibrary.wiley.com/doi/abs/10.1029/JD091iD09p09893.

Bouchut, F., 2007. Chapter 4: Efficient Numerical Finite Volume Schemes for Shallow Water Models. In: Zeitlin, V. (Ed.), Nonlinear Dynamics of Rotating Shallow Water: Methods and Advances. In: Edited Series on Advances in Nonlinear Science and Complexity, Vol. 2, Elsevier, pp. 189–256.

Bouchut, F., Lambaerts, J., Lapeyre, G., Zeitlin, V., 2009. Fronts and nonlinear waves in a simplified shallow-water model of the atmosphere with moisture and convection. Phys. Fluids 21 (11), 116604. http://dx.doi.org/10.1063/1.3265970.

Bouchut, F., Zeitlin, V., 2010. A robust well-balanced scheme for multi-layer shallow water equations. Discrete Contin. Dyn. Syst. B 13 (4), 739–758, URL https://www.aimsciences.org/article/id/cd9d0b2d-0da7-4c0a-9a41-970cca03d63a.

Brown, S., Janssen, M., Adumitroaie, V., Atreya, S., Bolton, S., Gulkis, S., Ingersoll, A., Levin, S., Li, C., Li, L., Lunine, J., Misra, S., Orton, G., Steffes, P., Tabataba-Vakili, F., Kolmašová, I., Imai, M., Santolík, O., Kurth, W., Hospodarsky, G., Gurnett, D., Connerney, J., 2018. Prevalent lightning sferics at 600 megahertz near Jupiter's poles. Nature 558 (7708), 87–90. http://dx.doi.org/10.1038/s41586-018-0156-5.

Cao, Y., Kurganov, A., Liu, Y., Zeitlin, V., 2024. Flux globalization-based well-balanced path-conservative central-upwind scheme for two-dimensional two-layer thermal rotating shallow water equations. J. Comput. Phys. 515, 113273, URL https://www.sciencedirect.com/science/article/pii/S0021999124005217.

Cartwright, D., 1978. Oceanic tides. The International Hydrographic Review.

Chemke, R., Kaspi, Y., 2015. Poleward migration of eddy-driven jets. J. Adv. Modelling Earth Syst. 7 (3), 1457–1471, URL https://agupubs.onlinelibrary.wiley.com/doi/abs/10.1002/2015MS000481.

Cosentino, R.G., Butler, B., Sault, B., Morales-Juberías, R., Simon, A., de Pater, I., 2017. Atmospheric waves and dynamics beneath Jupiter's clouds from radio wavelength observations. Icarus 292, 168–181, URL https://www.sciencedirect.com/science/article/pii/S0019103516304900.

de Pater, I., Sault, R.J., Butler, B., DeBoer, D., Wong, M.H., 2016. Peering through Jupiter's clouds with radio spectral imaging. Science 352 (6290), 1198–1201, URL https://www.science.org/doi/abs/10.1126/science.aaf2210.

Del Genio, A.D., McGrattan, K.B., 1990. Moist convection and the vertical structure and water abundance of Jupiter's atmosphere. Icarus 84 (1), 29–53, URL http://www.sciencedirect.com/science/article/pii/0019103590901564.

Dowling, T.E., 1994. Successes and failures of shallow-water interpretations of Voyager wind data. Chaos 4 (2), 213–225. http://dx.doi.org/10.1063/1.166005.

Dowling, T.E., Bradley, M.E., Colón, E., Kramer, J., LeBeau, R.P., Lee, G.C., Mattox, T.I., Morales-Juberías, R., Palotai, C.J., Parimi, V.K., Showman, A.P., 2006. The EPIC atmospheric model with an isentropic/terrain-following hybrid vertical coordinate. Icarus 182 (1), 259–273, URL https://www.sciencedirect.com/science/article/pii/S0019103506000303.

Dowling, T., Fischer, A., Gierasch, P., Harrington, J., LeBeau, R., Santori, C., 1998. The explicit planetary isentropic-coordinate (EPIC) atmospheric model. Icarus 132 (2), 221–238, URL https://www.sciencedirect.com/science/article/pii/S0019103598959176.

Dowling, T.E., Ingersoll, A.P., 1989. Jupiter's great red spot as a shallow water system. J. Atmos. Sci. 46 (21), 3256–3278, URL https://journals.ametsoc.org/view/journals/atsc/46/21/1520-0469_1989_046_3256_jgrsaa_2_0_co_2.xml.

Duer, K., Galanti, E., Kaspi, Y., 2020. The range of Jupiter's flow structures that fit the Juno asymmetric gravity measurements. J. Geophys. Res.: Planets 125 (8), e2019JE006292, URL https://agupubs.onlinelibrary.wiley.com/doi/abs/10.1029/2019JE006292.

Emanuel, K.A., 1994. Atmospheric Convection. Oxford University Press.

Fletcher, L.N., Greathouse, T., Orton, G., Sinclair, J., Giles, R., Irwin, P., Encrenaz, T., 2016. Mid-infrared mapping of Jupiter's temperatures, aerosol opacity and chemical distributions with IRTF/TEXES. Icarus 278, 128–161, URL https://www.sciencedirect.com/science/article/pii/S0019103516302834.

García-Melendo, E., Arregi, J., Rojas, J., Hueso, R., Barrado-Izagirre, N., Gómez-Forrellad, J., Pérez-Hoyos, S., Sanz-Requena, J., Sánchez-Lavega, A., 2011. Dynamics of Jupiter's equatorial region at cloud top level from cassini and HST images. Icarus 211 (2), 1242–1257, URL https://www.sciencedirect.com/science/article/pii/S0019103510004392.

García-Melendo, E., Sánchez-Lavega, A., 2001. A study of the stability of jovian zonal winds from HST images: 1995–2000. Icarus 152 (2), 316–330, URL http://www.sciencedirect.com/science/article/pii/S0019103501966461.

Gibbard, S., Levy, E.H., Lunine, J.I., 1995. Generation of lightning in Jupiter's water cloud. Nature 378 (6557), 592–595. http://dx.doi.org/10.1038/378592a0.

Gierasch, P.J., Ingersoll, A.P., Banfield, D., Ewald, S.P., Helfenstein, P., Simon-Miller, A., Vasavada, A., Breneman, H.H., Senske, D.A., Team, G.I., 2000. Observation of moist convection in Jupiter's atmosphere. Nature 403 (6770), 628–630. http://dx.doi.org/10.1038/35001017.

Giles, R.S., Greathouse, T.K., Hue, V., Gladstone, G.R., Melin, H., Fletcher, L.N., Irwin, P.G.J., Kammer, J.A., Versteeg, M.H., Bonfond, B., Grodent, D.C., Bolton, S.J., Levin, S.M., 2021. Meridional variations of C2H2 in Jupiter's stratosphere from Juno UVS observations. J. Geophys. Res.: Planets 126 (8), e2021JE006928, URL https://agupubs.onlinelibrary.wiley.com/doi/abs/10.1029/2021JE006928.

Gill, A., 1980. Some simple solutions for heat induced tropical circulation. Q. J. R. Meteorol. Soc. 106, 447–462. http://dx.doi.org/10.1002/qj.49710644905.

Gill, A., 1982. Studies of moisture effects in simple atmospheric models: The stable case. Geophys. Astrophys. Fluid Dyn. 19, 119. http://dx.doi.org/10.1080/03091928208208950.

Gouzien, E., Lahaye, N., Zeitlin, V., Dubos, T., 2017. Thermal instability in rotating shallow water with horizontal temperature/density gradients. Phys. Fluids 29 (10), 101702. http://dx.doi.org/10.1063/1.4996981.

Grassi, D., Adriani, A., Mura, A., Atreya, S.K., Fletcher, L.N., Lunine, J.I., Orton, G.S., Bolton, S., Plainaki, C., Sindoni, G., Altieri, F., Cicchetti, A., Dinelli, B.M., Filacchione, G., Migliorini, A., Moriconi, M.L., Noschese, R., Olivieri, A., Piccioni, G., Sordini, R., Stefani, S., Tosi, F., Turrini, D., 2020. On the spatial distribution of minor species in Jupiter's troposphere as inferred from Juno JIRAM data. J. Geophys. Res.: Planets 125 (4), e2019JE006206, URL https://agupubs.onlinelibrary.wiley.com/doi/abs/10.1029/2019JE006206.

Guervilly, C., Cardin, P., 2017. Multiple zonal jets and convective heat transport barriers in a quasi-geostrophic model of planetary cores. Geophys. J. Int. 211 (1), 455–471. http://dx.doi.org/10.1093/gji/ggx315.

Guillot, T., 1995. Condensation of methane, ammonia, and water and the inhibition of convection in giant planets. Science 269 (5231), 1697–1699, URL http://www.jstor.org/stable/2888575.

Guillot, T., Li, C., Bolton, S.J., Brown, S.T., Ingersoll, A.P., Janssen, M.A., Levin, S.M., Lunine, J.I., Orton, G.S., Steffes, P.G., Stevenson, D.J., 2020a. Storms and the depletion of ammonia in Jupiter: II. Explaining the Juno observations. J. Geophys. Res.: Planets 125 (8), e2020JE006404, URL https://agupubs.onlinelibrary.wiley.com/doi/abs/10.1029/2020JE006404.

Guillot, T., Stevenson, D.J., Atreya, S.K., Bolton, S.J., Becker, H.N., 2020b. Storms and the depletion of ammonia in Jupiter: I. microphysics of "mushballs". J. Geophys. Res.: Planets 125 (8), e2020JE006403, URL https://agupubs.onlinelibrary.wiley.com/doi/abs/10.1029/2020JE006403.

Hess, S.L., Panofsky, H.A., 1951. The atmospheres of the other planets. In: Compendium of Meteorology: Prepared under the Direction of the Committee on the Compendium of Meteorology. American Meteorological Society, Boston, MA, pp. 391–398. http://dx.doi.org/10.1007/978-1-940033-70-9_34.

Hoskins, B.J., Bretherton, F.P., 1972. Atmospheric frontogenesis models: Mathematical formulation and solution. J. Atmos. Sci. 29 (1), 11–37. http://dx.doi.org/10.1175/1520-0469(1972)029<0011:AFMMFA>2.0.CO;2.

Hueso, R., Sánchez-Lavega, A., 2001. A three-dimensional model of moist convection for the giant planets: The Jupiter case. Icarus 151 (2), 257–274, URL http://www.sciencedirect.com/science/article/pii/S0019103500966065.

Hyder, A., Lyra, W., Chanover, N., Morales-Juberías, R., Jackiewicz, J., 2022. Exploring Jupiter's polar deformation lengths with high-resolution shallow water modeling. Planetary Sci. J. 3 (7), 166. http://dx.doi.org/10.3847/PSJ/ac7952.

Ingersoll, A.P., 1990. Atmospheric dynamics of the outer planets. Science 248 (4953), 308–315, URL https://science.sciencemag.org/content/248/4953/308.

Ingersoll, A.P., 2002. Atmospheric dynamics of the outer planets. In: Pearce, R. (Ed.), Meteorology at the Millennium. In: International Geophysics, Vol. 83, Academic Press, pp. 306–315, URL http://www.sciencedirect.com/science/article/pii/S0074614202801747.

Ingersoll, A., Beebe, R., Mitchell, J.L., Garneau, G., Yagi, G.M., Muller, J., 1981. Interaction of eddies and mean zonal flow on Jupiter as inferred from Voyager 1 and 2 images. J. Geophys. Res. 86, 8733–8743.

Ingersoll, A.P., Cuzzi, J.N., 1969. Dynamics of Jupiter's cloud bands. J. Atmos. Sci. 26 (5), 981–985. http://dx.doi.org/10.1175/1520-0469(1969)026<0981:DOJCB>2.0.CO;2.

Ingersoll, A.P., Gierasch, P.J., Banfield, D., Vasavada, A.R., Team, G.I., 2000. Moist convection as an energy source for the large-scale motions in Jupiter's atmosphere. Nature 403 (6770), 630–632. http://dx.doi.org/10.1038/35001021.

Iñurrigarro, P., Hueso, R., Legarreta, J., Sánchez-Lavega, A., Eichstädt, G., Rogers, J., Orton, G., Hansen, C., Pérez-Hoyos, S., Rojas, J., Gómez-Forrellad, J., 2020. Observations and numerical modelling of a convective disturbance in a large-scale cyclone in Jupiter's south temperate belt. Icarus 336, 113475, URL https://www.sciencedirect.com/science/article/pii/S0019103519302970.

Jones, C.A., Rotvig, J., Abdulrahman, A., 2003. Multiple jets and zonal flow on Jupiter. Geophys. Res. Lett. 30 (14), URL https://agupubs.onlinelibrary.wiley.com/doi/abs/10.1029/2003GL016980.

Kaspi, Y., Flierl, G.R., Showman, A.P., 2009. The deep wind structure of the giant planets: Results from an anelastic general circulation model. Icarus 202 (2), 525–542, URL https://www.sciencedirect.com/science/article/pii/S0019103509001225.

Kaspi, Y., Galanti, E., Hubbard, W.B., Stevenson, D.J., Bolton, S.J., Iess, L., Guillot, T., Bloxham, J., Connerney, J.E.P., Cao, H., Durante, D., Folkner, W.M., Helled, R., Ingersoll, A.P., Levin, S.M., Lunine, J.I., Miguel, Y., Militzer, B., Parisi, M., Wahl, S.M., 2018. Jupiter's atmospheric jet streams extend thousands of kilometres deep. Nature 555 (7695), 223–226. http://dx.doi.org/10.1038/nature25793.

Kaspi, Y., Galanti, E., Showman, A.P., Stevenson, D.J., Guillot, T., Iess, L., Bolton, S.J., 2020. Comparison of the deep atmospheric dynamics of Jupiter and Saturn in light of the Juno and Cassini gravity measurements. Space Sci. Rev. 216 (5), 84. http://dx.doi.org/10.1007/s11214-020-00705-7.

Katsaros, K., 2001. Evaporation and humidity. In: Steele, J.H. (Ed.), Encyclopedia of Ocean Sciences. Academic Press, Oxford, pp. 870–877, URL http://www.sciencedirect.com/science/article/pii/B012227430X000684.

Kolmašová, I., Santolík, O., Imai, M., Kurth, W.S., Hospodarsky, G.B., Connerney, J.E.P., Bolton, S.J., Lán, R., 2023. Lightning at Jupiter pulsates with a similar rhythm as in-cloud lightning at Earth. Nature Commun. 14 (1), 2707. http://dx.doi.org/10.1038/s41467-023-38351-6.

Kong, D., Zhang, K., Schubert, G., Anderson, J.D., 2018. Origin of Jupiter's cloud-level zonal winds remains a puzzle even after Juno. Proc. Natl. Acad. Sci. 115 (34), 8499–8504, URL https://www.pnas.org/doi/abs/10.1073/pnas.1805927115.

Konor, C.S., Arakawa, A., 1997. Design of an atmospheric model based on a generalized vertical coordinate. Mon. Weather Rev. 125 (7), 1649–1673, URL https://journals.ametsoc.org/view/journals/mwre/125/7/1520-0493_1997_125_1649_doaamb_2.0.co_2.xml.

Kurganov, A., Liu, Y., Zeitlin, V., 2020. Moist-convective thermal rotating shallow water model. Phys. Fluids 32 (6), 066601. http://dx.doi.org/10.1063/5.0007757.

Lahaye, N., Zeitlin, V., 2012a. Decaying vortex and wave turbulence in rotating shallow water model, as follows from high-resolution direct numerical simulations. Phys. Fluids 24 (11), 115106. http://dx.doi.org/10.1063/1.4767723.

Lahaye, N., Zeitlin, V., 2012b. Existence and properties of ageostrophic modons and coherent tripoles in the two-layer rotating shallow water model on the f-plane. J. Fluid Mech. 706, 71–107. http://dx.doi.org/10.1017/jfm.2012.222.

Lahaye, N., Zeitlin, V., 2016. Understanding instabilities of tropical cyclones and their evolution with a moist convective rotating shallow–water model. J. Atmos. Sci. 73 (2), 505–523, URL https://journals.ametsoc.org/view/journals/atsc/73/2/jas-d-15-0115.1.xml.

Lambaerts, J., Lapeyre, G., Zeitlin, V., 2011a. Moist versus dry barotropic instability in a shallow-water model of the atmosphere with moist convection. J. Atmos. Sci. 68 (6), 1234–1252, URL https://journals.ametsoc.org/view/journals/atsc/68/6/2011jas3540.1.xml.

Lambaerts, J., Lapeyre, G., Zeitlin, V., 2012. Moist versus dry baroclinic instability in a simplified two-layer atmospheric model with condensation and latent heat release. J. Atmos. Sci. 69 (4), 1405–1426. http://dx.doi.org/10.1175/JAS-D-11-0205.1.

Lambaerts, J., Lapeyre, G., Zeitlin, V., Bouchut, F., 2011b. Simplified two-layer models of precipitating atmosphere and their properties. Phys. Fluids 23 (4), 046603. http://dx.doi.org/10.1063/1.3582356.

Le Sommer, J., Reznik, G.M., Zeitlin, V., 2004. Nonlinear geostrophic adjustment of long-wave disturbances in the shallow-water model on the equatorial beta-plane. J. Fluid Mech. 515, 135–170. http://dx.doi.org/10.1017/S0022112004000229.

Legarreta, J., Barrado-Izagirre, N., García-Melendo, E., Sánchez-Lavega, A., Gómez-Forrellad, J.M., IOPW Team, 2016. A large active wave trapped in Jupiter's equator. Astron. Astrophys. 586, A154. http://dx.doi.org/10.1051/0004-6361/201526197.

Lewis, J.S., 1969. The clouds of Jupiter and the NH3-H2O and NH3-H2S systems. Icarus 10 (3), 365–378, URL http://www.sciencedirect.com/science/article/pii/0019103569900918.

Li, C., Ingersoll, A.P., 2015. Moist convection in hydrogen atmospheres and the frequency of Saturn's giant storms. Nat. Geosci. 8 (5), 398–403. http://dx.doi.org/10.1038/ngeo2405.

Li, C., Ingersoll, A., Bolton, S., Levin, S., Janssen, M., Atreya, S., Lunine, J., Steffes, P., Brown, S., Guillot, T., Allison, M., Arballo, J., Bellotti, A., Adumitroaie, V., Gulkis, S., Hodges, A., Li, L., Misra, S., Orton, G., Oyafuso, F., Santos-Costa, D., Waite, H., Zhang, Z., 2020. The water abundance in Jupiter's equatorial zone. Nat. Astron. 4 (6), 609–616. http://dx.doi.org/10.1038/s41550-020-1009-3.

Li, C., Ingersoll, A., Janssen, M., Levin, S., Bolton, S., Adumitroaie, V., Allison, M., Arballo, J., Bellotti, A., Brown, S., Ewald, S., Jewell, L., Misra, S., Orton, G., Oyafuso, F., Steffes, P., Williamson, R., 2017. The distribution of ammonia on Jupiter from a preliminary inversion of Juno microwave radiometer data. Geophys. Res. Lett. 44 (11), 5317–5325, URL https://agupubs.onlinelibrary.wiley.com/doi/abs/10.1002/2017GL073159.

Limaye, S.S., 1986. Jupiter: New estimates of the mean zonal flow at the cloud level. Icarus 65 (2), 335–352, URL http://www.sciencedirect.com/science/article/pii/0019103586901429.

Lindzen, R.S., Batten, E.S., Kim, J.-W., 1968. Oscillations in atmospheres with tops. Mon. Weather Rev. 96 (3), 133–140, URL https://journals.ametsoc.org/view/journals/mwre/96/3/1520-0493_1968_096_0133_oiawt_2_0_co_2.xml.

Little, B., Anger, C.D., Ingersoll, A.P., Vasavada, A.R., Senske, D.A., Breneman, H., Borucki, W.J., The Galileo SSI Team, 1999. Galileo images of lightning on Jupiter. Icarus 142 (2), 306–323, URL http://www.sciencedirect.com/science/article/pii/S001910359996195X.

Liu, J., Goldreich, P.M., Stevenson, D.J., 2008. Constraints on deep-seated zonal winds inside Jupiter and Saturn. Icarus 196 (2), 653–664, URL https://www.sciencedirect.com/science/article/pii/S0019103508001371, Mars Polar Science IV.

Mousis, O., Ronnet, T., Lunine, J.I., 2019. Jupiter's formation in the vicinity of the amorphous ice snowline. Astrophys. J. 875 (1), 9. http://dx.doi.org/10.3847/1538-4357/ab0a72.

Palotai, C., Dowling, T.E., 2008. Addition of water and ammonia cloud microphysics to the EPIC model. Icarus 194 (1), 303–326, URL https://www.sciencedirect.com/science/article/pii/S0019103507005088.

Porco, C.C., West, R.A., McEwen, A., Del Genio, A.D., Ingersoll, A.P., Thomas, P., Squyres, S., Dones, L., Murray, C.D., Johnson, T.V., Burns, J.A., Brahic, A., Neukum, G., Veverka, J., Barbara, J.M., Denk, T., Evans, M., Ferrier, J.J., Geissler, P., Helfenstein, P., Roatsch, T., Throop, H., Tiscareno, M., Vasavada, A.R., 2003. Cassini imaging of Jupiter's atmosphere, satellites, and rings. Science 299 (5612), 1541–1547, URL https://science.sciencemag.org/content/299/5612/1541.

Proudman, J., 1942. On Laplace's differential equations for the tides. Proc. R. Soc. Lond. A 179 (978), 261–288. http://dx.doi.org/10.1098/rspa.1942.0002.

Read, P.L., 2024. The dynamics of Jupiter's and Saturn's weather layers: A synthesis after Cassini and Juno. Annu. Rev. Fluid Mech. 56 (Volume 56, 2024), 271–293, URL https://www.annualreviews.org/content/journals/10.1146/annurev-fluid-121021-040058.

Ribstein, B., Plougonven, R., Zeitlin, V., 2014. Inertial versus baroclinic instability of the bickley jet in continuously stratified rotating fluid. J. Fluid Mech. 743, 1–31. http://dx.doi.org/10.1017/jfm.2014.26.

Ripa, P., 1993. Conservation laws for primitive equations models with inhomogeneous layers. Geophys. Astrophys. Fluid Dyn. 70 (1–4), 85–111. http://dx.doi.org/10.1080/03091929308203588.

Rogers, J.H., 1995. The Giant Planet Jupiter. Cambridge University Press, Cambridge; New York, NY, USA.

Rostami, M., Petri, S., Guimarães, S.O., Fallah, B., 2024a. Open-source stand-alone version of atmospheric model Aeolus 2.0 software. Geosci. Data J. 11 (4), 1086–1093, URL https://rmets.onlinelibrary.wiley.com/doi/abs/10.1002/gdj3.249.

Rostami, M., Severino, L., Petri, S., Hariri, S., 2024b. Dynamics of localized extreme heatwaves in the mid-latitude atmosphere: A conceptual examination. Atmos. Sci. Lett. 25 (1), e1188, URL https://rmets.onlinelibrary.wiley.com/doi/abs/10.1002/asl.1188.

Rostami, M., Zeitlin, V., 2017. Influence of condensation and latent heat release upon barotropic and baroclinic instabilities of vortices in a rotating shallow water f-plane model. Geophys. Astrophys. Fluid Dyn. 111 (1), 1–31. http://dx.doi.org/10.1080/03091929.2016.1269897.

Rostami, M., Zeitlin, V., 2018. An improved moist-convective rotating shallow-water model and its application to instabilities of hurricane-like vortices. Q. J. R. Meteorol. Soc. 144 (714), 1450–1462, URL https://rmets.onlinelibrary.wiley.com/doi/abs/10.1002/qj.3292.

Rostami, M., Zeitlin, V., 2019a. Eastward-moving convection-enhanced modons in shallow water in the equatorial tangent plane. Phys. Fluids 31 (2), 021701. http://dx.doi.org/10.1063/1.5080415.

Rostami, M., Zeitlin, V., 2019b. Geostrophic adjustment on the equatorial beta-plane revisited. Phys. Fluids 31 (8), 081702. http://dx.doi.org/10.1063/1.5110441.

Rostami, M., Zeitlin, V., 2020. Can geostrophic adjustment of baroclinic disturbances in the tropical atmosphere explain MJO events? Q. J. R. Meteorol. Soc. 146 (733), 3998–4013, URL https://rmets.onlinelibrary.wiley.com/doi/abs/10.1002/qj.3884.

Rostami, M., Zeitlin, V., 2021. Eastward-moving equatorial modons in moist-convective shallow-water models. Geophys. Astrophys. Fluid Dyn. 115 (3), 345–367. http://dx.doi.org/10.1080/03091929.2020.1805448.

Rostami, M., Zeitlin, V., 2022a. Evolution of double-eye wall hurricanes and emergence of complex tripolar end states in moist-convective rotating shallow water model. Phys. Fluids 34 (6), 066602. http://dx.doi.org/10.1063/5.0096554.

Rostami, M., Zeitlin, V., 2022b. Instabilities of low-latitude easterly jets in the presence of moist convection and topography and related cyclogenesis, in a simple atmospheric model. Geophys. Astrophys. Fluid Dyn. 116 (1), 56–77. http://dx.doi.org/10.1080/03091929.2021.1959574.

Rostami, M., Zeitlin, V., Montabone, L., 2018. On the role of spatially inhomogeneous diabatic effects upon the evolution of Mars' annular polar vortex. Icarus 314, 376–388, URL https://www.sciencedirect.com/science/article/pii/S0019103517306073.

Rostami, M., Zeitlin, V., Spiga, A., 2017. On the dynamical nature of Saturn's north polar hexagon. Icarus 297, 59–70, URL https://www.sciencedirect.com/science/article/pii/S0019103516305978.

Rostami, M., Zhao, B., Petri, S., 2022. On the genesis and dynamics of Madden–Julian oscillation-like structure formed by equatorial adjustment of localized heating. Q. J. R. Meteorol. Soc. 148 (749), 3788–3813, URL https://rmets.onlinelibrary.wiley.com/doi/abs/10.1002/qj.4388.

Rotvig, J., 2007. Multiple zonal jets and drifting: Thermal convection in a rapidly rotating spherical shell compared to a quasigeostrophic model. Phys. Rev. 76, 046306, URL https://link.aps.org/doi/10.1103/PhysRevE.76.046306.

Sánchez-Lavega, A., Montero, R.R., 1985. Ground based observations of synoptic cloud systems in southern equatorial to temperate latitudes of Jupiter from 1975 to 1983. Astron. Astrophys. 148, 67–78, URL https://api.semanticscholar.org/CorpusID:120174930.

Sankar, R., Palotai, C., 2022. A new convective parameterization applied to Jupiter: Implications for water abundance near the 24°N region. Icarus 380, 114973, URL https://www.sciencedirect.com/science/article/pii/S0019103522000902.

Schecter, D.A., Dunkerton, T.J., 2009. Hurricane formation in diabatic Ekman turbulence. Q. J. R. Meteorol. Soc. 135 (641), 823–838, URL https://rmets.onlinelibrary.wiley.com/doi/abs/10.1002/qj.405.

Schneider, T., Liu, J., 2009. Formation of jets and equatorial superrotation on Jupiter. J. Atmos. Sci. 66 (3), 579–601, URL https://journals.ametsoc.org/view/journals/atsc/66/3/2008jas2798.1.xml.

Showman, A.P., 2007. Numerical simulations of forced shallow-water turbulence: Effects of moist convection on the large-scale circulation of Jupiter and Saturn. J. Atmos. Sci. 64 (9), 3132–3157, URL https://journals.ametsoc.org/view/journals/atsc/64/9/jas4007.1.xml.

Simon, A.A., 1999. The structure and temporal stability of Jupiter's zonal winds: A study of the North Tropical Region. Icarus 141 (1), 29–39, URL http://www.sciencedirect.com/science/article/pii/S0019103599961638.

Simon, A.A., Beebe, R.F., Gierasch, P.J., Vasavada, A.R., Belton, M.J., 1998. Global context of the Galileo-E6 observations of Jupiter's white ovals. Icarus 135 (1), 220–229, URL http://www.sciencedirect.com/science/article/pii/S001910359895970X.

Simon-Miller, A.A., Rogers, J.H., Gierasch, P.J., Choi, D., Allison, M.D., Adamoli, G., Mettig, H.-J., 2012. Longitudinal variation and waves in Jupiter's south equatorial wind jet. Icarus 218 (2), 817–830, URL http://www.sciencedirect.com/science/article/pii/S0019103512000371.

Smith, B.A., Soderblom, L.A., Johnson, T.V., Ingersoll, A.P., Collins, S.A., Shoemaker, E.M., Hunt, G.E., Masursky, H., Carr, M.H., Davies, M.E., Cook, A.F., Boyce, J., Danielson, G.E., Owen, T., Sagan, C., Beebe, R.F., Veverka, J., Strom, R.G., McCauley, J.F., Morrison, D., Briggs, G.A., Suomi, V.E., 1979. The Jupiter system through the eyes of Voyager 1. Science 204 (4396), 951–972, URL https://science.sciencemag.org/content/204/4396/951.

Smith, C.A., Speer, K.G., Griffiths, R.W., 2014. Multiple zonal jets in a differentially heated rotating annulus. J. Phys. Oceanogr. 44 (9), 2273–2291, URL https://journals.ametsoc.org/view/journals/phoc/44/9/jpo-d-13-0255.1.xml.

Thomson, S.I., 2020. The influence of deep jets on Jupiter's weather layer in a 1.5-layer shallow-water model. Q. J. R. Meteorol. Soc. 146 (729), 1608–1625, URL https://rmets.onlinelibrary.wiley.com/doi/abs/10.1002/qj.3755.

Tollefson, J., Wong, M.H., de Pater, I., Simon, A.A., Orton, G.S., Rogers, J.H., Atreya, S.K., Cosentino, R.G., Januszewski, W., Morales-Juberías, R., Marcus, P.S., 2017. Changes in Jupiter's zonal wind profile preceding and during the Juno mission. Icarus 296, 163–178, URL https://www.sciencedirect.com/science/article/pii/S0019103517301641.

Tyler, R.H., 2022. Jupiter's banding and jets may be caused by tides. Planetary Sci. J. 3 (11), 250. http://dx.doi.org/10.3847/PSJ/ac8f91.

Vasil, G.M., Lecoanet, D., Burns, K.J., Oishi, J.S., Brown, B.P., 2019. Tensor calculus in spherical coordinates using Jacobi polynomials. Part-I: mathematical analysis and derivations. J. Comput. Phys.: X 3, 100013, URL https://www.sciencedirect.com/science/article/pii/S2590055219300290.

Wang, D., Lunine, J.I., Mousis, O., 2016. Modeling the disequilibrium species for Jupiter and Saturn: Implications for Juno and Saturn entry probe. Icarus 276, 21–38, URL https://www.sciencedirect.com/science/article/pii/S0019103516300951.

Weidenschilling, S., Lewis, J., 1973. Atmospheric and cloud structures of the Jovian planets. Icarus 20 (4), 465–476, URL http://www.sciencedirect.com/science/article/pii/0019103573900195.

Williams, G., 2003. Jovian dynamics. Part III: Multiple, migrating, and equatorial jets. J. Atmos. Sci. 60 (10), 1270–1296, URL https://journals.ametsoc.org/view/journals/atsc/60/10/1520-0469_2003_60_1270_jdpimm_2.0.co_2.xml.

Williams, G.P., Wilson, R.J., 1988. The stability and genesis of Rossby vortices. J. Atmos. Sci. 45 (2), 207–241, URL https://journals.ametsoc.org/view/journals/atsc/45/2/1520-0469_1988_045_0207_tsagor_2_0_co_2.xml.

Williams, G.P., Yamagata, T., 1984. Geostrophic regimes, intermediate solitary vortices and Jovian eddies. J. Atmos. Sci. 41 (4), 453–478, URL https://journals.ametsoc.org/view/journals/atsc/41/4/1520-0469_1984_041_0453_grisva_2_0_co_2.xml.

Yair, Y., Levin, Z., Tzivion, S., 1995. Lightning generation in a Jovian thundercloud: Results from an axisymmetric numerical cloud model. Icarus 115 (2), 421–434, URL http://www.sciencedirect.com/science/article/pii/S0019103585711086.

Young, R.M., Read, P.L., Wang, Y., 2019. Simulating Jupiter's weather layer. Part I: Jet spin-up in a dry atmosphere. Icarus 326, 225–252, URL https://www.sciencedirect.com/science/article/pii/S0019103518304391.

Zeitlin, V., 2018. Geophysical Fluid Dynamics: Understanding (almost) Everything with Rotating Shallow Water Models. Oxford University Press, Oxford, xix+488.

Zhao, B., Zeitlin, V., Fedorov, A.V., 2021. Equatorial modons in dry and moist-convective shallow-water systems on a rotating sphere. J. Fluid Mech. 916, A8. http://dx.doi.org/10.1017/jfm.2021.159.